Article

Developmental Cell

An Excitable Ras/PI3K/ERK Signaling Network Controls Migration and Oncogenic Transformation in Epithelial Cells

Graphical Abstract

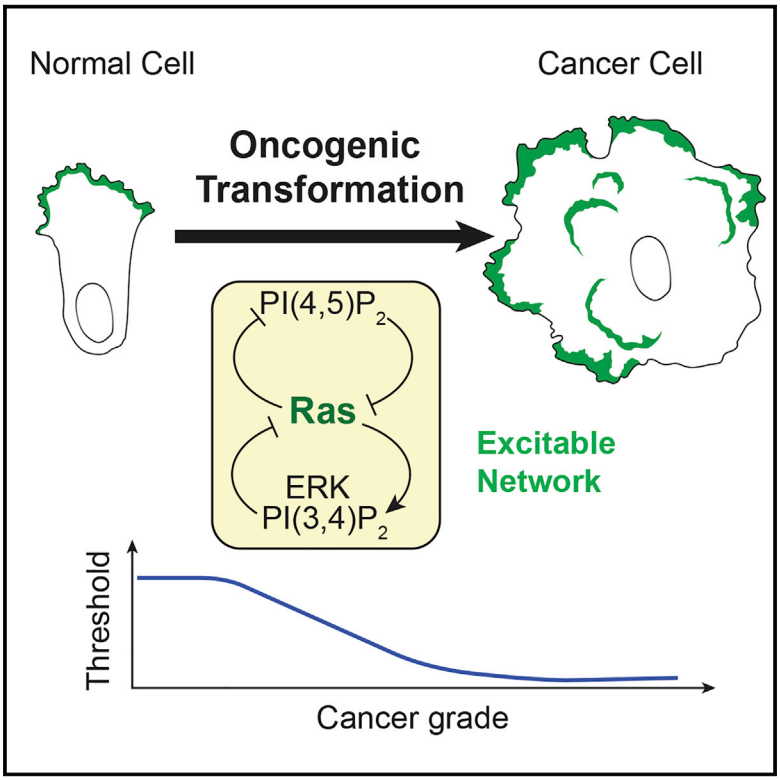

Authors

Huiwang Zhan, Sayak Bhattacharya, Huaqing Cai, Pablo A. Iglesias, Chuan-Hsiang Huang, Peter N. Devreotes

Correspondence

chuang29@jhmi.edu (C.-H.H.), pnd@jhmi.edu (P.N.D.)

In Brief

Zhan et al., investigate the excitability of the Ras/PI3K/ERK signaling network. They demonstrate that activities propagate as coordinated waves on the cell cortex and delineate the molecular feedbacks that cause excitability. Transformed cells display more waves suggesting that cancer can be viewed as a low-threshold state of the network.

Highlights

- The Ras/PI3K/ERK network displays features of excitable systems in epithelial cells
- Network perturbations can increase the wave activity and the frequency of ERK pulses
- Wave activity is increased in transformed cells and increasingly metastatic cancer cells
- Cancer progression is a shift to a lower threshold of the excitable signaling network

Zhan et al., 2020, Developmental Cell *54*, 608–623
September 14, 2020
https://doi.org/10.1016/j.devcel.2020.08.001

CellPress

CellPress

Developmental Cell

Article

An Excitable Ras/PI3K/ERK Signaling Network Controls Migration and Oncogenic Transformation in Epithelial Cells

Huiwang Zhan,[1,2] Sayak Bhattacharya,[3] Huaqing Cai,[4] Pablo A. Iglesias,[2,3] Chuan-Hsiang Huang,[5,*] and Peter N. Devreotes[1,2,6,*]

[1]Department of Biological Chemistry, School of Medicine, Johns Hopkins University, Baltimore, MD 21205, USA
[2]Department of Cell Biology and Center for Cell Dynamics, School of Medicine, Johns Hopkins University, Baltimore, MD 21205, USA
[3]Department of Electrical and Computer Engineering, Whiting School of Engineering, Johns Hopkins University, Baltimore, MD 21218, USA
[4]National Laboratory of Biomacromolecules, Chinese Academy of Sciences Center for Excellence in Biomacromolecules, Institute of Biophysics, Chinese Academy of Sciences, Beijing 100101, China
[5]Department of Pathology, School of Medicine, Johns Hopkins University, Baltimore, MD 21205, USA
[6]Lead Contact
*Correspondence: chuang29@jhmi.edu (C.-H.H.), pnd@jhmi.edu (P.N.D.)
https://doi.org/10.1016/j.devcel.2020.08.001

SUMMARY

The Ras/PI3K/extracellular signal-regulated kinases (ERK) signaling network plays fundamental roles in cell growth, survival, and migration and is frequently activated in cancer. Here, we show that the activities of the signaling network propagate as coordinated waves, biased by growth factor, which drive actin-based protrusions in human epithelial cells. The network exhibits hallmarks of biochemical excitability: the annihilation of oppositely directed waves, all-or-none responsiveness, and refractoriness. Abrupt perturbations to Ras, PI(4,5)P2, PI(3,4)P2, ERK, and TORC2 alter the threshold, observations that define positive and negative feedback loops within the network. Oncogenic transformation dramatically increases the wave activity, the frequency of ERK pulses, and the sensitivity to EGF stimuli. Wave activity was progressively enhanced across a series of increasingly metastatic breast cancer cell lines. The view that oncogenic transformation is a shift to a lower threshold of excitable Ras/PI3K/ERK network, caused by various combinations of genetic insults, can facilitate the assessment of cancer severity and effectiveness of interventions.

INTRODUCTION

Studies of the signal transduction and cytoskeletal events involved in rapid morphological changes primarily in *Dictyostelium* cells have led to the "excitable network hypothesis." It proposes that self-organizing excitable signal transduction activities at the cell cortex provide global control of actomyosin-based protrusions that underlie cell dynamics. External chemical and biomechanical stimuli can guide cells and be integrated by influencing the overall threshold of the network (Gerisch et al., 2004; Weiner et al., 2007; Arai et al., 2010; Xiong et al., 2010; Huang et al., 2013; Taniguchi et al., 2013; Nishikawa et al., 2014; Tang et al., 2014; Miao et al., 2017; Yang et al., 2018; Pal et al., 2019). The generality of this hypothesis and its ability to explain transitions of cell behavior, such as oncogenic transformation, remains to be tested.

Among the patterns that excitable systems can display are propagating waves on two-dimensional surfaces, and the waves of cytoskeletal events have indeed been observed in a variety of cells. Traveling actin waves were initially discovered and have been extensively investigated in *Dictyostelium* cells (Vicker, 2002; Inagaki and Katsuno, 2017). Waves of SCAR/WAVE and F-actin steer the movement of neutrophils (Weiner et al., 2007; Wang et al., 2014; Yang et al., 2016). Additional examples include F-actin waves in mast cells (Wu et al., 2018), in spreading lymphocytes and macrophages (Lam Hui et al., 2014), in breast cancer cells (Marchesin et al., 2015), in *Xenopus* oocytes (Bement et al., 2015), in fish keratocytes (Barnhart et al., 2017), and in extending neuronal axons (Winans et al., 2016), and integrin waves in osteosarcoma cells (Case and Waterman, 2011).

Studies in *Dictyostelium* cells suggest that the waves of cytoskeletal activity are driven by a signal transduction excitable network (STEN), which involves Ras family proteins (Ras) and PI3-kinases (PI3K). These signal transduction responses display features of biochemical excitability, namely, "all-or-nothing" behavior to suprathreshold stimuli and refractory period to repeated stimuli (Huang et al., 2013; Tang et al., 2014). Lowering or raising the threshold of the excitable network can alter the cellular protrusions and cell migration modes (Miao et al., 2017, 2019). However, the extent to which the excitability of signaling transduction network controls cytoskeletal activities in mammalian cells and whether the molecular interactions in these networks are conserved throughout evolution is unknown.

Elucidating the quantitative properties of the signaling networks controlling cell morphology is critical for understanding

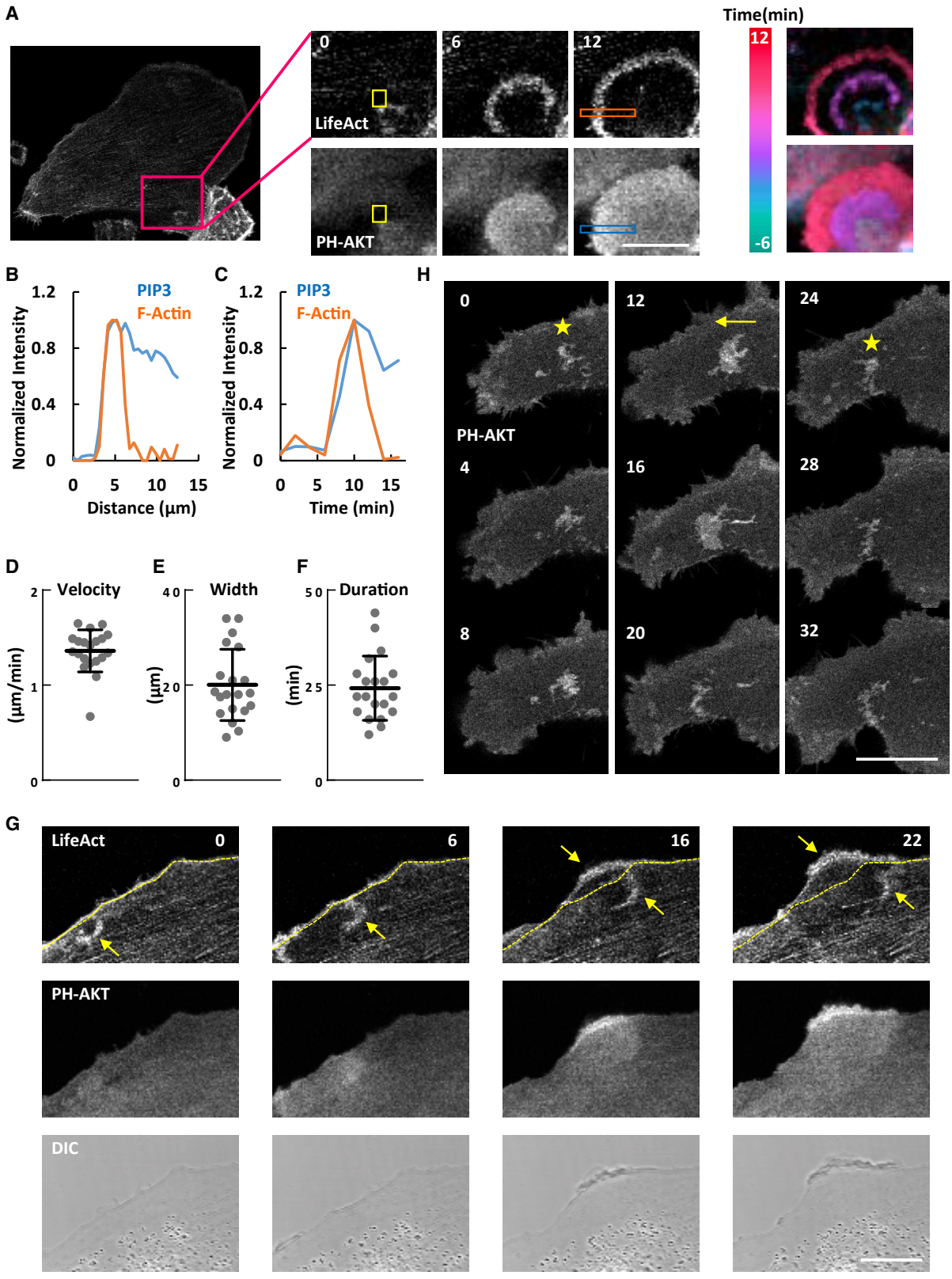

Figure 1. Cytoskeletal and Signaling Activities Propagate as Waves on the Basal Surface of the MDA-MB-231 Cell

(A) Confocal images focusing onto the ventral surface of the MDA-MB-231 cell expressing biosensors for F-actin (LifeAct-RFP [red fluorescent protein]) and PIP3 (PH-AKT-GFP) (also see Video S1). Color-coded overlays show the progression of waves as a function of time.

(legend continued on next page)

and treating cancer. The Ras/PI3K/extracellular signal-regulated kinases (ERK) signaling network is frequently mutated in cancer and leads to oncogenic transformation (Basolo et al., 1991; Imbalzano et al., 2009; Liu et al., 2009). It is known that the excess activation of a single oncogene, such as *Kras* is able to trigger hundreds of protein interactions and signaling feedbacks during transformation (Ye et al., 2016; Martinko et al., 2018). However, there is a lack of systems-level understanding of how these interactions and feedbacks are intrinsically regulated, which largely explains the poor outcome of clinical practices that target various single components of the signaling networks.

These considerations prompted us to investigate the excitable properties of the Ras/PI3K/ERK network in human epithelial cells, and the role of excitability in oncogenic transformation. We surveyed a series of mammalian cell lines and found that MDA-MB-231 cancer-derived cells displayed traveling Ras-PI3K-F-actin waves on the basal surface. We examined MDA-MB-231 cells and non-tumorigenic mammary cell line MCF-10A for evidence of biochemical excitability and the capacity of perturbations to alter these events and cellular protrusions. Both cell lines displayed all-or-nothing responsiveness and refractory periods. External stimuli and acute synthetic perturbations altered wave and/or protrusion behaviors as well as ERK pulse frequency. These observations allowed us to delineate feedback loops that bring about excitability. Furthermore, the activation of Ras enhanced wave activity in MDA-MB-231 cells, triggered *de novo* wave activity in MCF-10A cells, and increased protrusions in both. The invasive behavior across a series of increasingly metastatic breast cancer cell lines strongly correlates with elevated wave activity. Taken together, these studies suggest that excitable Ras/PI3K/ERK network as a driver of cellular protrusions is a general property of migrating cells and that the cellular transformation can be considered as a shift to a lower threshold or set point of these networks.

RESULTS

Coupled Signal Transduction and Cytoskeleton Waves Drive Protrusions

To monitor signal transduction and cytoskeleton activities at the ventral surface of MDA-MB-231 cells, we co-expressed biosensors for F-actin (LifeAct) and PIP3 (PH-AKT). As shown in Figure 1A and Video S1, the signal transduction and cytoskeleton activities initiated spontaneously and propagated as waves along the basal membrane. The activities were highly coordinated; the leading edge and peak of the actin and PIP3 waves coincided. Whereas the cytoskeletal wave was confined to 5 μm, the lagging edge of the signal transduction wave was broader (Figure 1B). Similarly, as the waves passed, the signal transduction and cytoskeleton activities initially increased in parallel and peaked at about 5 min. The cytoskeletal activity returned to basal within about 5 min while the signal transduction activity lasted longer (Figure 1C). The velocity of the traveling waves was 1.36 ± 0.22 μm/min (mean ± SD, n = 20) (Figure 1D). Many of the coupled F-actin and PIP3 waves started within the ventral surface and died out before reaching the edge of these large cells. The maximal lateral expansion of the waves was 20.05 ± 7.51 μm (mean ± SD, n = 20) with a duration of 24.20 ± 8.43 min (mean ± SD, n = 20) (Figures 1E and 1F). When a wave reached the edge of the cell, a ruffle strongly labeled with LifeAct and PH-AKT formed. This suggests that protrusions in epithelial cells are driven by coordinated PIP3 and F-actin waves (Figure 1G; Video S1).

In some instances, traveling waves stopped their forward progression and "hovered" in place. Figure 1H and Video S1 show an example of a PIP3 wave, which displayed some dynamic changes but did not propagate laterally for about 12 min. Then the wave began to propagate and continued for about 12 min before it stopped again. After about 8 min, it started to propagate again.

Signal Transduction and Cytoskeletal Networks Are Excitable

Previous studies in migrating *Dictyostelium* amoebae demonstrated that signal transduction and cytoskeletal activities display features of excitable systems, including mutually annihilating waves, all-or-none responses, and the existence of a refractory period (Gerisch et al., 2004; Huang et al., 2013). The following results indicate that an excitable system underlies the signaling and cytoskeletal waves in MDA-MB-231. First, when two oppositely propagating waves of LifeAct merged (3.5 min in Figure 2A, upper panel), they did not cross but instead merged and disappeared (7.1 and 10.6 min in Figure 2A, upper panel; Video S2). Similar annihilation was also observed for colliding waves of PH-AKT (Figure 2A, lower panel).

Second, we examined ERK activation and PIP3 production, two downstream effectors of Ras, in response to EGF stimuli of increasing dose and duration. We detected ERK activation by the nuclear exit of its biosensor ERK-KTR (Regot et al., 2014) in response to EGF. Stimuli of 5, 15, and 50 pg/mL induced ~15%, ~70%, and ~90% of cells to start intermittent ERK activation (showing at least a 50% increase) (Figures 2B–2D), similar to previously reported (Albeck et al., 2013). In addition, MCF10A cells had an elevated PIP3 in response to 1 and 5 min, but rarely to 30 s, saturating EGF stimuli (Figure 2E). Notably, the response started after the removal of 1 min stimulus and proceeded to completion (Figure 2E). Moreover, the magnitude and kinetics of the average responses to 1 or 5 min stimuli were nearly identical (Figures 2E and 2F). A similar duration threshold was obtained in MDA-MB-231 cells (Figures 2G and 2H). The behavior was very "cooperative": fitting the peak response versus the duration to the sigmoidal curve yielded Hill coefficients over 30 for both

(B) Relative amount of F-actin and PIP3 across the orange and blue boxes scan in (A).
(C) Temporal change of F-actin and PIP3 in the yellow boxes in (A).
(D–F) Distribution of the velocity (D), maximum width (E) and duration (F) among waves (mean ± SD of n = 20 waves in one cell).
(G) Example of a circular wave with one edge propagating outward to drive the formation of a protrusion upon reaching the cell perimeter (arrow indicates wave and dashed line indicates initial cell perimeter) (also see Video S1).
(H) Time-lapse confocal images of PH-AKT showing transitions between standing (marked with a star) and traveling (marked with an arrow) waves (also see Video S1).
The unit of time labeled on images is min and scale bar is 20 μm.

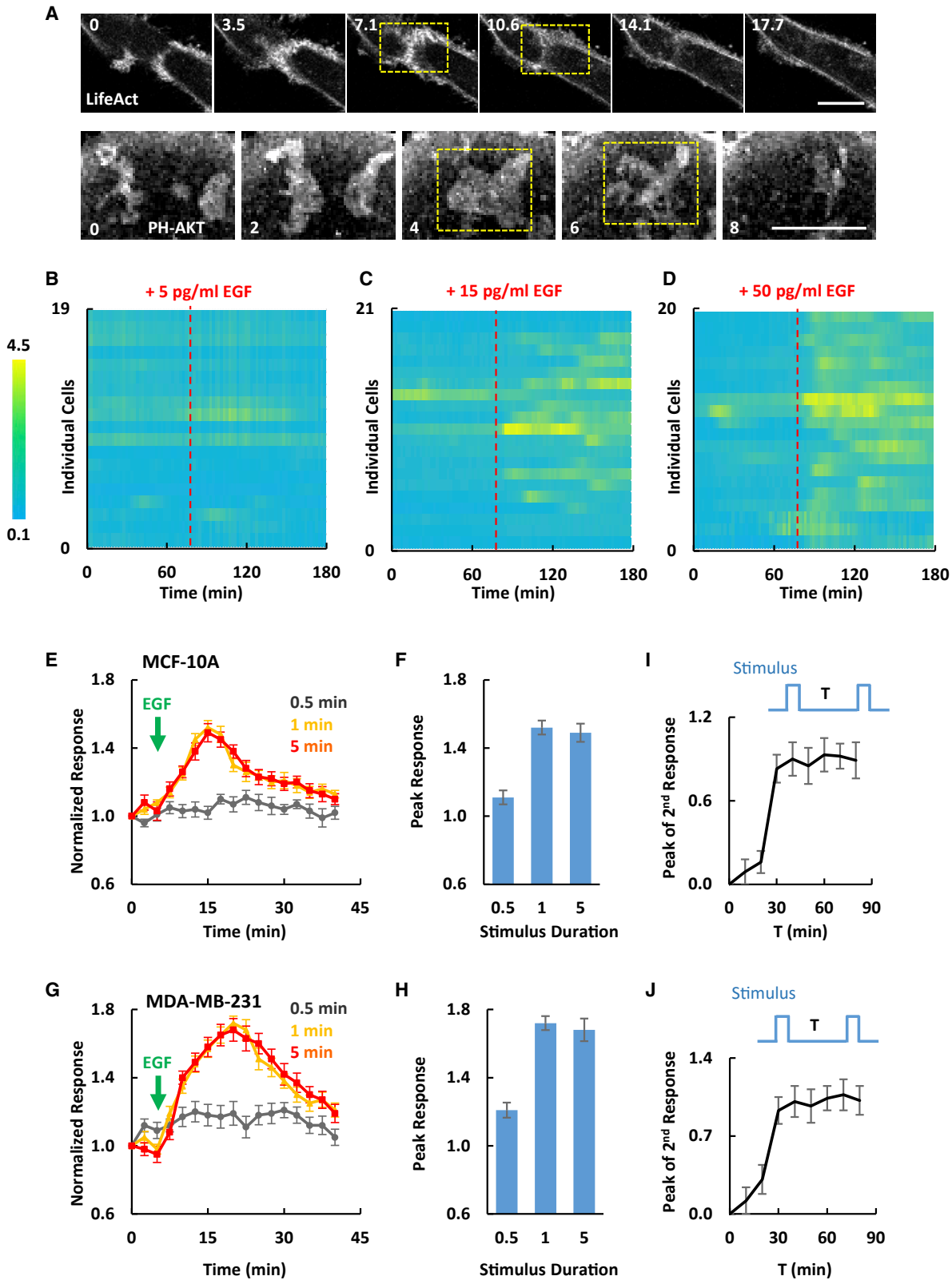

(legend on next page)

MCF10A and MDA-MB-231. These observations suggested that stimuli crossing a threshold can trigger full responses.

Third, we applied paired 1 min stimuli separated by various intervals. The second stimulus failed to trigger a full response unless a sufficient recovery time was allowed, suggesting the existence of a refractory period (Figures 2I, 2J, and S1A). In both cell types, the kinetics of the recovery showed an initial lag of about 10 min, and the magnitude of the second response was half-maximal after 25 min of recovery. Taken together, these observations indicate that cytoskeletal and signaling activities in MCF-10A and MDA-MB-231 cells indeed display salient features of excitable systems.

Exogenous EGF Perturbs Signal Transduction and Cytoskeletal Waves

We examined the effects of uniform and gradient EGF stimuli on wave behavior. When an MDA-MB-231 cell was given a uniform EGF stimulus, the coupled F-actin and PIP3 waves initially disappeared and were replaced by a bright ring of signal around the cell perimeter. After about 50 min, waves began to reappear in the central region as the edge signal decreased (Figures 3A and 3B; Video S3). Eventually, they were more prevalent than those in cells prior to stimulation. The temporal evolution of the responses over the peripheral and interior regions was evident in kymographs of cropped images (Huang et al., 2013) (Figure 3C). We next used an EGF-filled micropipette to generate a spatial gradient of stimulation. At the steady-state, PH-AKT waves that formed toward the high side of the EGF gradient were wider, more intense, and longer-lasting than those closer to the low side of the gradient (Figures 3D–3F; Video S3).

Building on a previously published mathematical model of the excitable signaling network (Xiong et al., 2010), we were able to simulate the responses of cells to uniform and gradient stimuli. In the two-dimensional simulation, prior to stimulation, spontaneous waves were triggered by noise. A uniform stimulus induced a global response followed by a brief period of inactivity before the waves were reinitiated (Figure 3G; Video S4). These results are generally in agreement with responses observed in MDA-MB-231 cells except that the global response in live cells was primarily seen at the perimeter rather than across the basal surface (Figure 3A). With a gradient stimulus, more abundant and wider waves were generated close to the high side of the gradient (Figure 3H; Video S4), consistent with the observations in Figure 3D.

A Small Decrease in PI(4,5)P2 Activates the Signal Transduction Network and Lowers the Threshold of the Network

PI(4,5)P2, as the substrate of the reaction, is reduced during the production of PI(3,4,5)P3 (PIP3) by the activated Ras-PI3K network. We therefore tested how acute perturbations to PI(4,5)P2 reduction affect excitability in MCF-10A and MDA-MB-231 cells. To rapidly lower the level of PI(4,5)P2, we recruited the 5-phosphatase, Inp54p, using chemically induced dimerization (CID) (Figure S1B). Membrane recruitment of Inp54p caused an immediate reduction of PI(4,5)P2, detected by the translocation of the PI(4,5)P2-binding domain PH-PLCΔ, from the membrane to the cytoplasm (Figure S1C). Recruitment of a catalytically inactive mutant Inp54p (D281A) did not affect PH-PLCΔ localization (Figure S1D).

In MCF-10A cells, PI(4,5)P2 reduction triggered two distinct types of responses: spreading or retraction (Figure S2A). Spreading cells increased their basal surface area and showed ruffles, whereas retracting cells formed blebs around the cell perimeter. We noticed that, compared with retracting cells, the spreading cells had lower expression levels of Inp54p (Figure S2B), suggesting that the type of response depends on the extent of PI(4,5)P2 reduction. To test this possibility, we observed individual cells exposed to increasing doses of rapamycin. Whereas a low dose (5 nM) of rapamycin caused a slight increase in cytosolic PH-PLCΔ and strong cell spreading, a subsequent higher dose (1 μM) of rapamycin caused a further increase in cytosolic PH-PLCΔ, which led to contraction (Figures S2C and S2D). Moreover, when cells were sorted according to the intensity of Inp54p fluorescence, most of the low or high expressers, respectively, spread or retracted (Figures S2E and S2F). Cells expressing a catalytically inactive Inp54p mutant did not respond to rapamycin addition (Figure S2F).

The morphological changes induced by the modest lowering of PI(4,5)P2 in MCF-10A cells were dynamic and associated with biochemical responses. Within minutes of the addition of rapamycin, peripheral regions of the cell began to spread rhythmically (Figure 4A; Video S5). Kymographs of the length of the lamellipodia revealed that the protrusions propagated around the perimeter with a period of about 20 min, suggesting that they are driven by scroll waves (Figure 4B). The protrusions were labeled with RBD (biosensor for active Ras) (Figures 4C, 4D, and S3A; Video S5) and PH-AKT (Figure S3B), indicating that locally elevated Ras and the PI3K activity at protrusions drove the oscillatory spreading. The overall activity of Ras also increased when PI(4,5)P2 was lowered (Figures 4E and 4F). Elevated PIP3 production on cell protrusions by PI(4,5)P2 lowering was also detected in cells treated with JLY (Figures S4A–S4D), a cocktail of cytoskeletal inhibitors used to block the cell shape changes (Peng et al., 2011), suggesting that the cytoskeletal activity is not required for the activation of signaling. We next examined the downstream effectors of these activities. Immunofluorescence staining revealed a wide band of S473-AKT phosphorylation (Figure S3C), indicating the activation of

Figure 2. The Signaling Network Is Excitable

(A) Two colliding actin or PIP3 waves in MDA-MB-231 cells annihilated (dashed yellow boxes) (also see Video S2).

(B–D) Responses of ERK-KTR to EGF stimulation of different concentrations in MCF-10A cells. Ratios of cytosolic to nucleus ERK-KTR signal were plotted over time for 19, 21, and 20 cells in one experiment as shown in (B), (C), and (D). EGF stimulations were applied at 78 min.

(E–H) Quantification of PIP3 responses to 0.5, 1, and 5 min saturated EGF stimuli in MCF-10A (E and F) and MDA-MB-231 (G and H) cells (mean ± SEM of n = 10 cells of 3 experiments).

(I and J) Peak responses to the second of two 1 min stimuli separated by interval T in MCF-10A (I) and MDA-MB-231 (J) cells (mean ± SEM of n = 10 cells of 3 experiments). An example of the individual cell response is shown in Figure S1A.

Cells were starved in pure DMEM/F-12 (MCF-10A) or DMEM (MDA-MB-231) medium for 24 h before EGF stimulation. The unit of time labeled on images is min and scale bar is 20 μm.

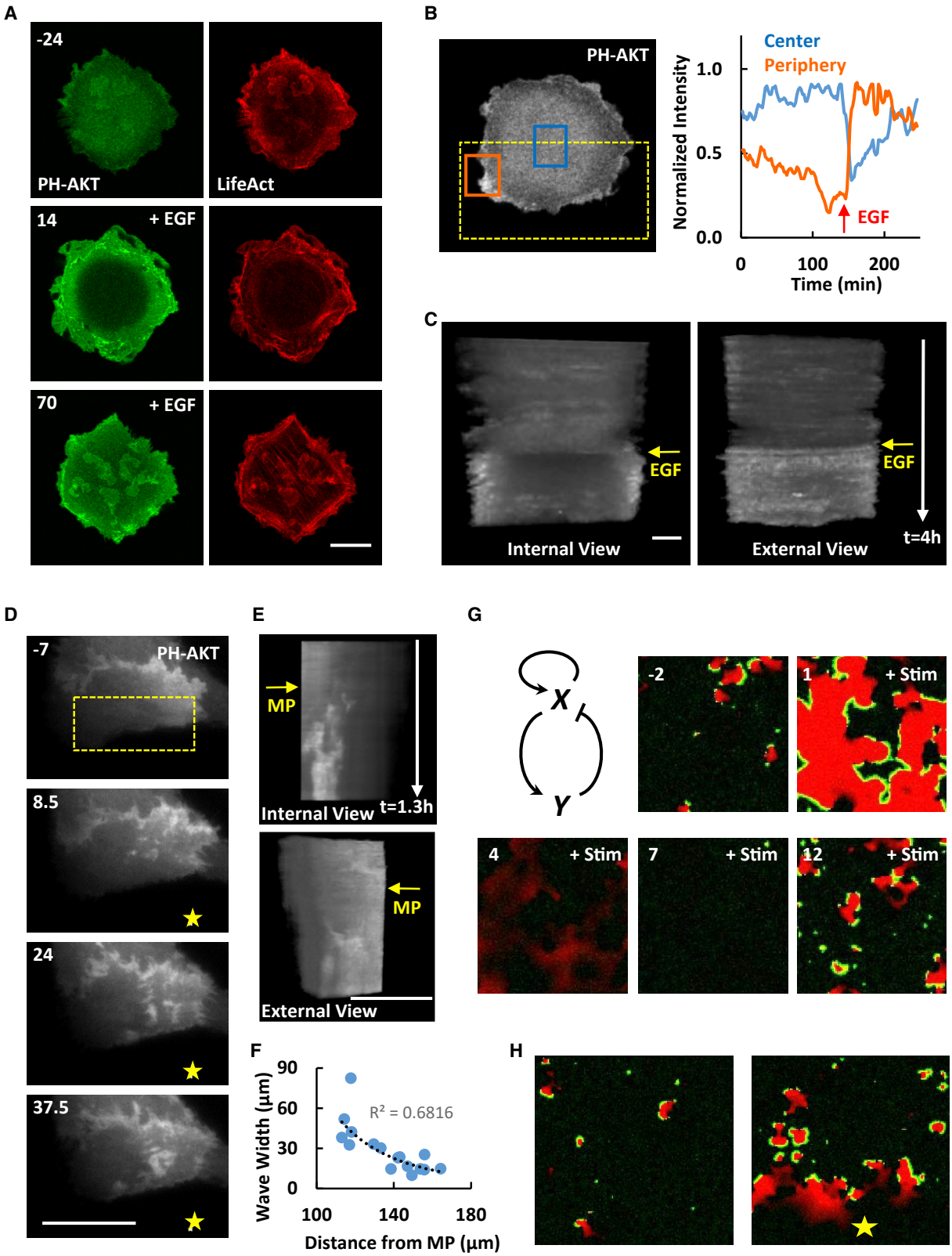

Figure 3. Global and Local Stimuli Change the Activity of Cytoskeletal and Signaling Waves

(A) Confocal images of the MDA-MB-231 cell showing the response of PIP3 and actin waves to global EGF stimulation (2 ng/mL, added at 0 min) (also see Video S3). Cells were starved in pure DMEM medium for 2 h before EGF stimulation.

(legend continued on next page)

mTORC2 at the protrusions (Manning and Toker, 2017). We also noticed that lowering of PI(4,5)P2 triggered ERK activation (Figures 4G and 4H; Video S5). The extent of ERK activation within the cell population was heterogeneous (Figure 4I). Furthermore, during continuous stimulation, the elevated steady-state level fluctuated (Figures 4H and 4I). Together, the results indicate that PI(4,5)P2 lowering activates the Ras signaling network, which leads to the activation of multiple downstream events.

In MDA-MB-231 cells, slight PI(4,5)P2 lowering led to more PH-AKT and RBD waves in the interior regions of the basal cell surface and more ruffles at the cell edge. The increase in waves covering the basal surface was due to both *de novo* initiation as well as growth in pre-existing waves (Figures 4J–4L; Video S6). The temporal evolution of these waves is demonstrated by the t stack of a section throughout the images (Figure S3D) (Huang et al., 2013). Patches of PIP3 or RBD appeared in the interior upon rapamycin addition, indicating a new wave formation. PIP3- or RBD-enriched oscillatory protrusions also appeared on the perimeter. As in MCF-10A cells, a slight decrease of PI(4,5)P2 mostly caused spreading, while a large depletion of PI(4,5)P2 caused retraction and blebbing in MDA-MB-231 cells (Figure S3E).

Theoretically, in excitable systems, the amount of spontaneous activity depends on the set point or threshold of the system. The generation of dynamic protrusions in MCF-10A cells and traveling waves in MDA-MB-231 cells suggested that PI(4,5)P2 lowering decreased the threshold of the excitable signaling network. To test this idea, we compared EGF-triggered ERK responses of MCF-10A cells in the presence or absence of PI(4,5)P2 lowering. PI(4,5)P2 lowering led to a greater percentage of cells responding to sub-saturating EGF stimulation (Figures 5A–5E). When stimulated with increasing levels of EGF, the dose-response curve of PI(4,5)P2-reduced cells was left-shifted relative to that of the control cells (Figure 5F). Together, these results suggested that a slight PI(4,5)P2 reduction lowers the threshold of the Ras-PI3K excitable signaling network and this is reflected in a greater sensitivity of ERK in EGF stimulation.

mTORC2 Links Signal Transduction and Cytoskeletal Activities

To further define the mediators of the morphological changes induced by PI(4,5)P2 reduction, we blocked key pathways downstream of Ras using small molecule inhibitors. PI3K inhibitor ZSTK474 caused retraction of protrusions and reduced the wave activities in unstimulated MDA-MB-231 cells (Figures S4E–S4I). The morphological changes induced by PI(4,5)P2 reduction still occurred in the presence of the PI3K inhibitor. In contrast, MCF-10A cells treated with PP242, which had abolished S473-AKT phosphorylation (Figure S5A), the PI(4,5)P2 lowering-induced cell spreading response was blocked (Figures S5C, S5D, and 6A). Consistently, the response was also blocked by the knocking down of mTOR (mammalian target of rapamycin) with shRNA (Figures S5E, S5G, S5H, and 6B). We do not believe that this effect is due to the inhibition of mTORC1, since, as noted above, mTORC1 specific inhibitor rapamycin did not alter the cell spreading behavior. It was further confirmed by the result that shRictor also blocked the cell spreading response induced by decreasing PI(4,5)P2 (Figures S5F, S5G, S5I, and 6B). Together, these results suggest that the effects of PI(4,5)P2 reduction on cytoskeletal activity act through a pathway involving mTORC2.

ERK and PI(3,4)P2 Are Negative Regulators in the Excitable Network

Since ERK is activated by PI(4,5)P2 lowering (Figures 4G–4I), we tested the role of ERK in mediating the spreading response. Surprisingly, the ERK inhibitor Ulixertinib alone caused more cell spreading (Figure 6C). Subsequent lowering of PI(4,5)P2 after ERK inhibition caused no further increase in cell spreading (Figure 6D). This suggests that the major role of ERK is as a negative regulator of the system (Figure 6L).

Recent evidence suggests that PI(3,4)P2 has physiological roles in addition to being a product of PIP3 degradation (Gewinner et al., 2009; Hawkins and Stephens, 2016; Guo et al., 2016; Malek et al., 2017; Li et al., 2018; Goulden et al., 2019). We compared the dynamic levels of PIP3 and PI(3,4)P2 using biosensors PH-AKT and PH-TAPP1. While PIP3 and PI(3,4)P2 both localized on cell protrusions, they were spatially separated. PIP3 formed a band at the perimeter, whereas PI(3,4)P2 formed a trailing band back from the perimeter in both MCF-10A and MDA-MB-231 cells (Figures 6E–6G and S6A–S6C).

We next measured the kinetics of PIP3 and PI(3,4)P2 changes in response to 2 ng/mL EGF in MCF-10A cells. Upon stimulation, PIP3 and PI(3,4)P2 increased globally on the membrane. PIP3 reached a peak within 2 min, while PI(3,4)P2 rose more slowly and peaked 1 min later (Figure 6H). The difference in the kinetics is consistent with the spatial relationship seen in propagating waves and protrusions.

To determine the role of PI(3,4)P2 in the excitable network, we assessed the effects of acute reduction of PI(3,4)P2. We used CID to recruit INPP4B to hydrolyze PI(3,4)P2. Upon the addition of rapamycin, MCF-10A cells began to carry out oscillatory spreading, consistent with an increase in wave activity (Figures 6I, 6J, and S6D). This contrasted strikingly to the effects of

(B) Quantification of PIP3 change at the center (blue box) or periphery (orange box) of the cell ventral surface in (A).
(C) Internal and external views of stacked frames of ROI (dashed yellow box) in (B).
(D) Response of PIP3 wave to local EGF stimulation. Yellow star indicates the position of micropipette (filled with 10 μg/mL EGF, applied at 0 min). Also see Video S3. Cells were starved in pure DMEM medium for 2 h before EGF stimulation.
(E) Internal and external views of stacked frames of ROI (dashed yellow box) in (D).
(F) Wave maximum width versus distance to the micropipette in (D). The dashed black line is the power trend line.
(G) Computational simulation of waves response to global stimulus based on an activator-inhibitor scheme. Green is activator (X) while red is inhibitor (Y). Global stimulus was added at time 0 (a.u.) (also see Video S4).
(H) Computational simulation of waves response to local stimulus. Green is activator while red is inhibitor. Yellow star indicates the position of stimulus (also see Video S4).
The unit of time labeled on images is min and scale bar is 20 μm.

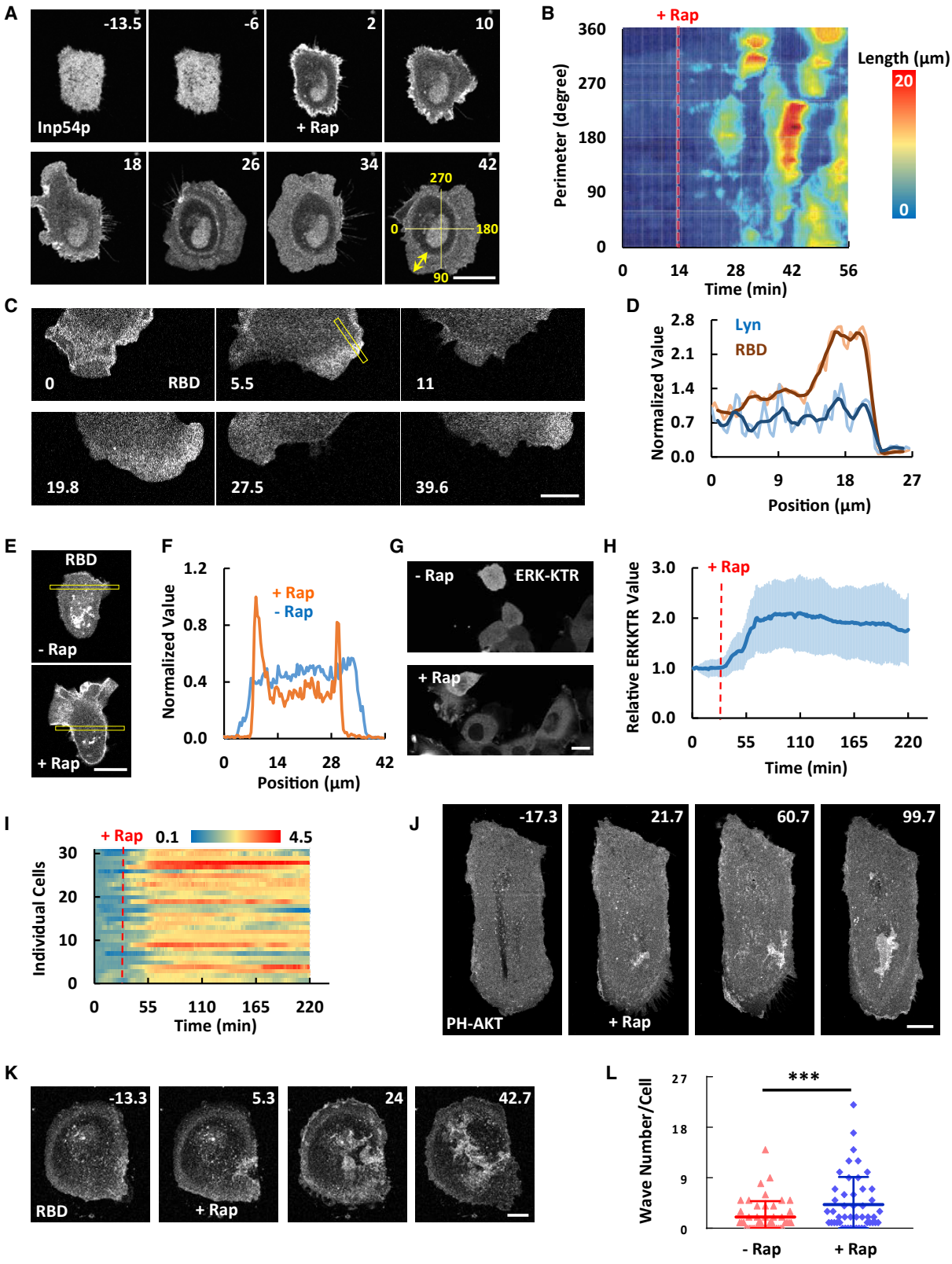

Figure 4. PI(4,5)P2 Reduction Changes Cell Morphology and Signaling Responses

(A) Time-lapse confocal images of MCF-10A cell expressing Lyn-FRB and FK506 binding protein (FKBP)-Inp54p (channel shown). 1 μM rapamycin was added at 0 min (also see Video S5).

(legend continued on next page)

PIP3 depletion, which caused cell retraction (Figures S4E and S4I). Furthermore, the morphological changes caused by PI(3,4)P2 reduction were accompanied by Ras activation as detected by its biosensor RBD (Figures 6K, S6E, and S6F). Together, these results suggest that PI(3,4)P2, activated following Ras and PI3K activation, provides a negative feedback loop to Ras activity (Figure 6L).

Oncogenic Transformation Causes Enhanced Excitability of the Signal Transduction Network

We examined the effect of the Ras activation on network excitability and cell morphology. If the network outlined in Figure 6L is correct, an increase in Ras activity would be expected to lower the threshold and lead to increased excitability. To acutely activate Ras, we used CID to rapidly recruit the CAAX-deleted constitutively active Kras_G12V to membrane-anchored Lyn-FRB upon rapamycin addition. In MCF-10A cells, Kras_G12V recruitment led to an oscillatory cell spreading, similar to the effects of PI(4,5)P2 reduction (Figure 7A). The effects of recruiting Ras-GEF, CDC25, were similar to those induced by Kras_G12V (Figure 7B). In order to examine the effect of Ras activation on existing wave activities, we recruited CDC25 in MDA-MB-231 cells. As indicated by the PIP3 biosensor PH-AKT, activation of Ras led to an increase in the number of traveling waves on the basal surface of the cells (Figure 7C; Video S7). As we have shown earlier, these changes are indicative of a lowered threshold of the STEN.

To directly correlate the excitability of the signaling network with cell oncogenic transformation, we examined MCF-10A cells expressing *Hras*, *Kras*, or C-MYC oncogenes. These cells have been shown to display features of cell transformation, including growth on soft agar (Basolo et al., 1991), epithelial to mesenchymal transition (Liu et al., 2009), and tumor formation in mouse xenografts (Imbalzano et al., 2009). In our hands, similar to PI(4,5)P2 lowering, the transformed cells were larger and more spread (Figure 7D) and showed lower resistance to hypotonic shock (Figure S7B). Expression of LifeAct, PH-AKT, and RBD revealed traveling actin, PIP3, and Ras waves moving across the basal surface of the transformed cells, as seen in MDA-MB-231 cells (Figures 7D and S7C–S7F; Video S7). As noted earlier, basal waves within the cell perimeter were rarely detected in control MCF-10A cells (Figure 7D). Transformed cells displayed a variety of concentric or spiral waves as well as intermittent standing and traveling waves. Some waves initiated at the perimeter with one side of the wave propagating inward and the other pushing the cell edge outward (Figure S7E). Other waves started interiorly, traveled to the edge, and pushed out. In four experiments, 41.8% ± 5.9% (mean ± SEM) of transformed cells and 5.9 ± 1.5 % (mean ± SEM) of control cells displayed these internal waves (Figure 7E). The transformed cell population had more spread cells than control MCF-10A cells; however, both small and large transformed cells displayed more waves and there was only a moderate correlation with cell size (R^2 = 0.4443) (Figures S7G and S7H). Furthermore, compared with the control, spontaneous ERK activity increased and showed more frequent oscillations in Ras_G12V transformed cells (Figures 7F and 7G). Since the increase in wave activity suggested that the threshold of the network is lowered, we examined the response of ERK to EGF stimulation with different doses in control and Kras_G12V cells. As shown in Figure S7I, the baseline activity of ERK was higher and the EC_{50} concentration of EGF needed to trigger responses was lower in the transformed cells. These results are consistent with the lowering of the threshold of STEN in PI(4,5)P2-reduced cells.

We next examined the wave activity in a series of cells derived from MCF-10A with increased metastatic potential, designated M1, M2, M3, and M4 cells. Whereas M1 and M2 correspond to wild-type and Ras-transformed cells, M3 and M4 cells were selected for higher metastatic index (Dawson et al., 1996; Santner et al., 2001; Weiger et al., 2013). We found that the wave activities of M1 and M2 were similar to our findings with the wild-type and Ras-transformed cells. In contrast, M3 and M4 displayed even more internal basal waves than M2 cells (Figure 7H; Video S7). Up to ~80% of M3 and ~90% of M4 cells displayed waves (Figure 7I). This observation suggested a strong correlation between wave activities on the basal surface of cells and metastatic potential.

DISCUSSION

Our studies provide systems-level mechanisms for migratory transitions and oncogenic transformation in human epithelial cells. We found that, first, these cells display propagating waves of Ras and PI3K activation and that waves reaching the cell perimeter drive protrusions. External stimulation with growth factors can influence the wave behavior. Second, oppositely directed waves merge and display mutual annihilation, and responses to growth factor display all-or-none responsiveness and refractory periods. Third, abrupt perturbations of Ras activity and phosphoinositide levels change the number and character of traveling waves and protrusions as well as the sensitivity to growth factor stimulation. These observations show that cellular protrusions are controlled by an excitable Ras/PI3K/

(B) Kymograph of lamellipodia length around the perimeter of the cell in (A). Quantification of cell area change is shown in Figure S2F.
(C) Time-lapse confocal images of the bottom surface of MCF-10A cell expressing Lyn-FRB (shown in Figure S3A), FKBP-Inp54p, and RBD (channel shown) after 1 μM rapamycin indicate active Ras enriched at the oscillatory protrusions. Also see Video S5.
(D) Quantification of the boxes scan in (C) and Figure S3A. The bold are the smoothed lines.
(E) Confocal images of the middle plane of MCF-10A cell expressing Lyn-FRB, FKBP-Inp54p, and RBD (channel shown) before and after 1 μM rapamycin.
(F) Quantification of the boxes scan in (E).
(G) Confocal images of MCF-10A cells expressing Lyn-FRB, FKBP-Inp54p, and ERK-KTR (channel shown) before and after 1 μM rapamycin (also see Video S5).
(H and I) Ratios of cytosolic to nucleus ERK-KTR signal in population average (H, mean ± SD of n = 31 cells in one experiment) and individual (I) MCF-10A cells.
(J and K) Time-lapse confocal images showing increased PIP3 waves (J, also see Video S6) or Ras waves (K, also see Video S6) formation after lowering PI(4,5)P2 in MDA-MB-231 cells. 1 μM rapamycin was added at 0 min. The t stack analysis of (J) is presented in Figure S3D.
(L) Quantification of wave number change in (J and K). Individual waves were followed from origin to end in videos. The total wave number for each cell was quantified during 1 h imaging windows before and after 1 μM rapamycin (mean ± SD of n = 48 cells, 5 experiments). Paired t test, p = 0.0004.
The unit of time labeled on images is min and scale bar is 20 μm.

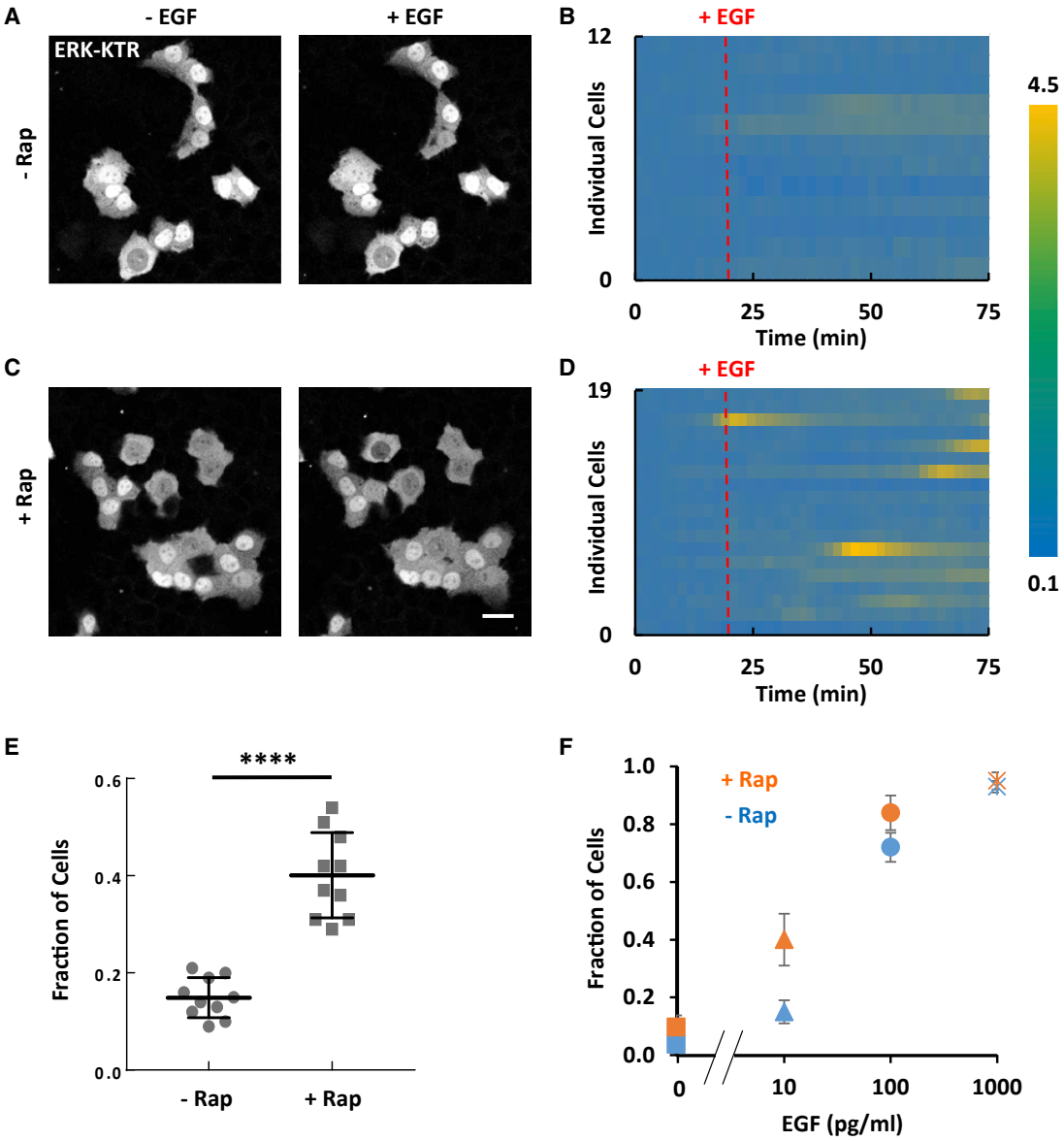

Figure 5. PI(4,5)P2 Reduction Lowers the Threshold of ERK Activation in MCF-10A Cells

(A–D) Responses of ERK-KTR to 10 pg/mL EGF stimulation in MCF-10A cells without (A and B) and with (C and D) PIP2 reduction by rapamycin-induced recruitment of Inp54p. Ratios of cytosolic to nucleus ERK-KTR signal over time for 12 and 19 individual cells are plotted in (B) and (D).

(E) Fraction of cells showing at least 50% increase in the ratio of cytosolic to nucleus intensity of ERK-KTR in response to 10 pg/mL EGF global stimulation with or without PIP2 reduction by rapamycin-induced recruitment of Inp54p (mean ± SD of n = 10 experiments). Unpaired t test with Welch's correction, $p < 0.0001$.

(F) Fraction of cells responding to global stimulation of various concentrations of EGF in cells without or with PIP2 reduction by rapamycin-induced recruitment of Inp54p (mean ± SD of n = 10 experiments).

Cells were starved in pure DMEM/F-12 medium for 24 h before stimulation. Scale bar labeled on images is 20 μm.

ERK network and that growth factors guide cells by locally altering excitability. They also delineate the feedback loops that contribute to excitability. Finally, we discovered that Ras transformation leads to *de novo* or increased wave activity, consistent with the increased protrusive activity displayed by transformed cells.

Multiple different criteria demonstrated that the downstream effectors of Ras, such as ERK and PI3K display properties of excitability in human epithelial cells. First, we repeated the observation that the oscillation of ERK activity can be promoted by EGF, as previously described in MCF-10A cells (Albeck et al., 2013). Second, there was no production of PIP3 to 30 s growth factor stimulation, while the responses to 1 and 5 min were quite similar. The responses to 1 and 5 min stimuli continued to increase after the stimuli were removed, suggesting that the system responds in an all-or-none fashion after crossing a threshold. Third, paired stimuli demonstrated the existence of a refractory period; cells required about 30 min to regain full

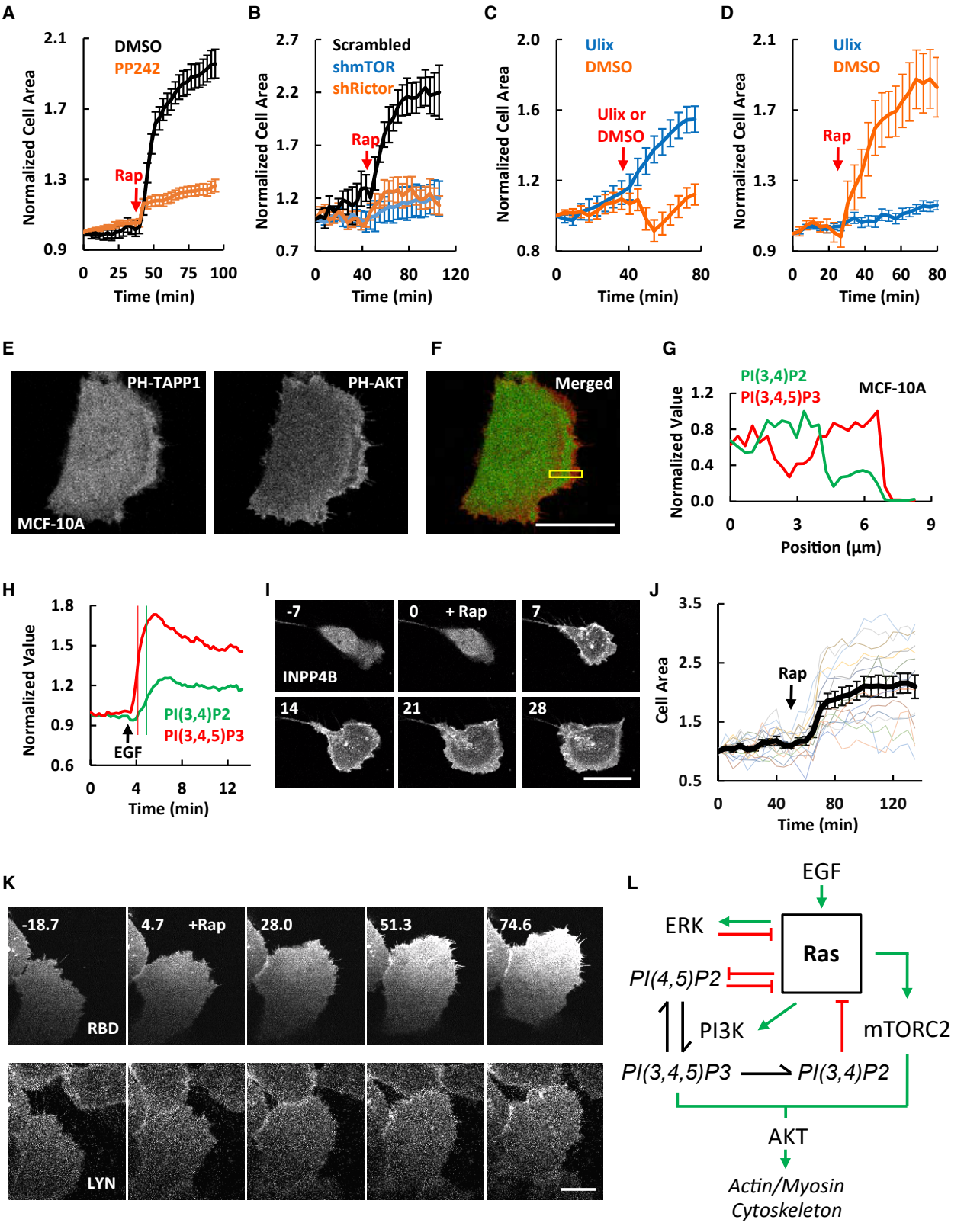

Figure 6. Molecular Mechanisms that Bring About Excitability

(A) Quantification of area changes of MCF-10A cells expressing Lyn-FRB and FKBP-Inp54 (images shown in Figures S5C and S5D) before and after 1 μM rapamycin (mean ± SEM of n = 15 cells of 5 experiments). Cells were either pre-treated with DMSO or 10 μM mTOR inhibitor PP242 for 2 h before imaging.

(legend continued on next page)

responsiveness. The refractory period explains why oppositely directed waves annihilate and the duration of the refractory period is consistent with the period of ERK oscillations.

The studies presented here show that actin waves in epithelial cells are regulated by a mechanism similar to that delineated in *Dictyostelium* (Vicker, 2002; Gerisch et al., 2004; Wozniak et al., 2005; Miao et al., 2017). In *Dictyostelium*, the slower kinetics of the signal transduction network lead to broad bands of Rap, Ras, and PI3K activity that move coordinately with leading and trailing peaks of F-actin polymerization. This behavior was attributed to the coupling of a slow STEN to a rapid cytoskeletal excitable network (CEN). These characteristics are apparently conserved in human epithelial cells reported here. We found that the previously reported actin "rosettes" (Marchesin et al., 2015) consisted of a narrow actin band accompanied by broader bands of Ras activation and PIP3. The duration of the responses is about 30 times longer, and the velocity of the waves is about 6 folds smaller, in epithelial versus ameboid cells. The different kinetics are consistent with the frequency and extension rate of protrusions as well as the speed of movements in the two different cells (Albeck et al., 2013; Aoki et al., 2013; Miao et al., 2019).

We also observed novel wave characteristics that had not been previously reported. First, we observed switching between traveling and standing waves, a recently predicted feature of excitable systems (Bhattacharya et al., 2020). Second, we found that the uniform growth factor triggered a global response, temporarily overwhelming wave activity, and that local gradients provided a directional bias to the waves in MDA-MB-231 cells. Our observations in MDA-MB-231 were closely simulated by manipulating the threshold in the STEN-CEN computational model. In *Dictyostelium*, the extent to which STEN activity can be biased by external stimuli appears to be context dependent and has been debated (Huang et al., 2013; Gerisch and Ecke, 2016). Our observations provide clear evidence to support the excitable network hypothesis with respect to cell guidance.

Our observations lead to a schematic view of the molecular identity of some of the feedback loops that bring about excitability (see Figure 6L). Ras is activated by EGF, which in turn activates ERK. ERK negatively regulates Ras activity. It has been reported that Ras activation reduces PI(4,5)P2 (Van Rheenen et al., 2007). We found that PI(4,5)P2 is a negative regulator of Ras activity, which would complete a mutually inhibitory positive feedback loop. PI(3,4)P2 as a product of PIP3 provides negative feedback to Ras. Finally, PIP3 together with mTORC2 provides a link through AKT to the cytoskeleton. Similar observations were previously made in *Dictyostelium* except that in amoebae resting PI(3,4)P2 levels are high and AKT can serve as a negative regulator of Ras activation. The consistent role of PI(3,4)P2 as a negative regulator in both systems is surprising, since PI(3,4)P2 is at the leading edge of the cell and generally considered as a positive regulator (Bae et al., 2010; Hansen and Mullins, 2015). However, our studies (Figures 6E–6G and S6A–S6C) and those in *Dictyostelium* (Li et al., 2018) indicate that PI(3,4)P2 at the leading edge lags behind PIP3. Other studies have pointed to additional feedback loops not assessed here. For instance, Ras, PI3K, the actin cytoskeleton, and cellular adhesion can form a positive feedback loop (Huang et al., 2013; Yang et al., 2018). Negative feedback involving myosin and AKT, as well as membrane tension and mTORC2 have been reported (Sasaki et al., 2007; Houk et al., 2012; Diz-Muñoz et al., 2016; Riggi et al., 2018).

Excitability of the Ras-PI3K network has important consequences in physiology and cancer. First, the excitable network can generate patterns, such as traveling waves of different dimensions or standing waves (Xiong et al., 2010; Bhattacharya et al., 2020). These patterns can generate a large repertoire of protrusions, such as pseudopodia, filopodia, lamellipodia, or invadopodia, and consequently explain a wide range of migratory behaviors (Huang et al, 2013; Taniguchi et al, 2013; Miao et al., 2017; Miao et al., 2019). Second, we found an increase in the wave and ERK activity in *Kras* transformed cells, as well as in cells where Ras was acutely activated. Furthermore, the increased wave activity was strongly correlated with metastatic potential across a series of increasingly aggressive breast cancer cell lines (M1∼M4 MCF10A cells). These suggest that the enhanced wave and ERK activities may control cell proliferation and cancer progression (Roberts and Der, 2007; Mebratu and Tesfaigzi, 2009; Mendoza et al., 2011; Serra et al., 2011; Samatar and Poulikakos, 2014; Tanimura and Takeda, 2017; Yang et al., 2018). Taken together, our studies suggest a novel view of oncogenic transformation as a shift to a lower threshold or set point of the Ras/PI3K/ERK excitable network. This change in threshold is manifested by an increase in stochastic noise-driven activities, such as the number and the range of propagating waves and

(B) Quantification of area changes of MCF-10A cells expressing Lyn-FRB and FKBP-Inp54p (images shown in Figures S5G–S5I) transfected with scrambled, mTOR, or Rictor shRNAs before and after 1 μM rapamycin (mean ± SEM of n = 20 cells of 5 experiments).
(C) Quantification of area changes of MCF-10A cells before and after treated with DMSO or 10 μM Ulixertinib (ERK inhibitor) (mean ± SEM of n = 20 cells for Ulix and 22 for DMSO of 3 experiments).
(D) Quantification of area changes of MCF-10A cells before and after rapamycin-induced PIP2 reduction (mean ± SEM of n = 18 cells for Ulix and 17 for DMSO of 3 experiments). Cells were either pre-treated with DMSO or 10 μM Ulixertinib for 2 h before imaging.
(E) Confocal images of MCF-10A cells expressing PH-TAPP1-GFP and PH-AKT-RFP.
(F) Merged images of both fluorescence channels in (E). Green is PH-TAPP1 and red is PH-AKT.
(G) Quantification of the boxes scan in (F). Similar results for MDA-MB-231 cells are shown in Figures S6A–S6C.
(H) PI(3,4)P2 and PI(3,4,5)P3 responses to global EGF (2 ng/mL) stimulation in MCF-10A cell. Thin vertical lines mark 50% values. Cells were starved in pure DMEM/F-12 medium for 24 h before EGF stimulation.
(I) Time-lapse confocal images of MCF-10A cell expressing Lyn-FRB and FKBP-INPP4B (channel shown). 1 μM rapamycin was added at 0 min.
(J) Quantification of the cell area changes of individual MCF-10A cells (colored lines) or population average (black line, mean ± SEM of n = 15 cells of 3 experiments) before and after rapamycin-induced PI(3,4)P2 reduction. The phosphatase inactive control is shown in Figure S6D.
(K) Time-lapse confocal images of the ventral surface of MCF-10A cell expressing Lyn-FRB (channel shown), FKBP-INPP4B, and RBD (channel shown). 1 μM rapamycin was added at 0 min. Quantification is shown in Figures S6E and S6F.
(L) Diagram of the working model. Green arrows indicate activating interactions while red bars indicate inhibitory interactions.
The unit of time labeled on images is min and scale bar is 20 μm.

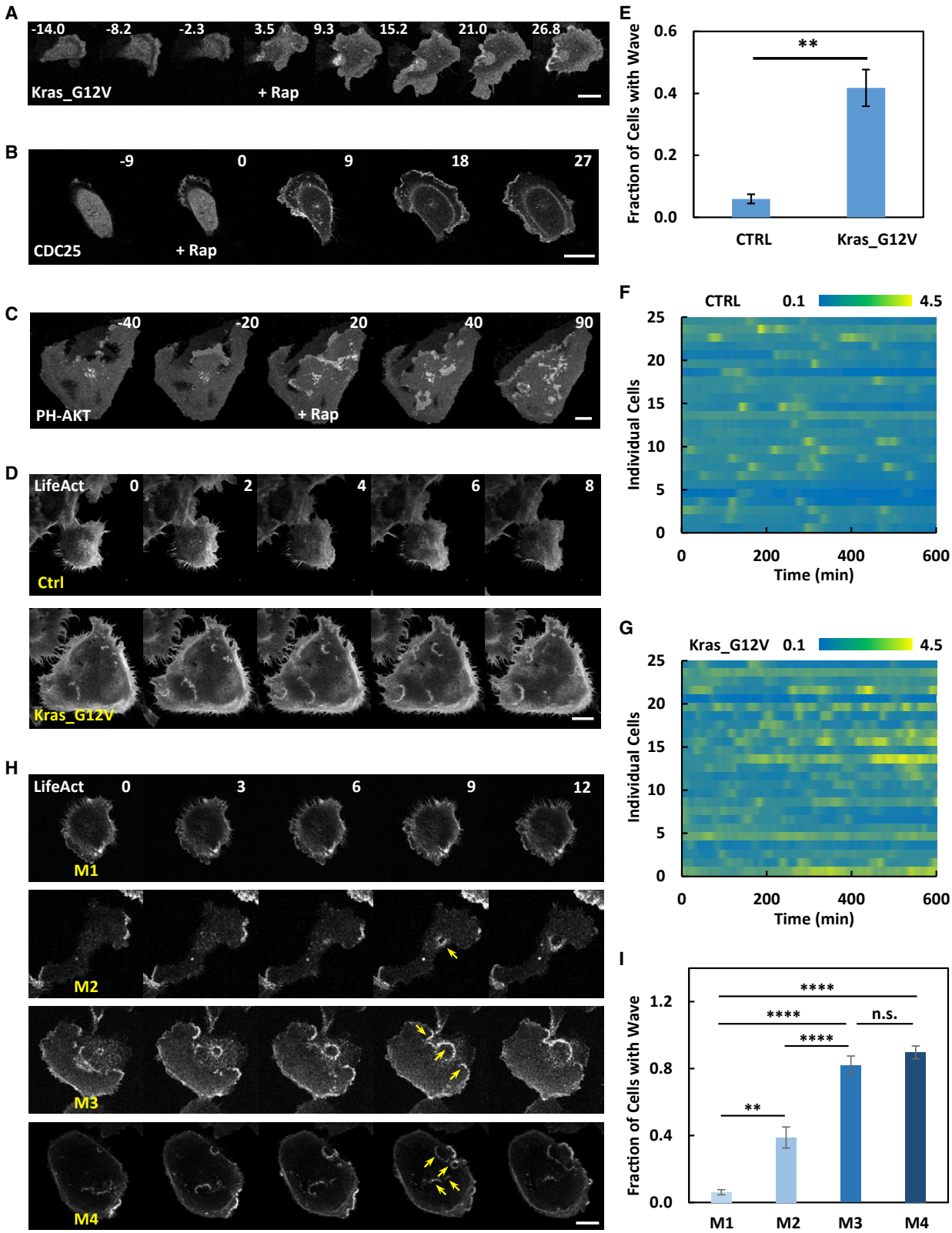

Figure 7. Oncogenic Transformation Causes Enhanced Excitability of the Signal Transduction Network

(A) Time-lapse confocal images of MCF-10A cell expressing Lyn-FRB and FKBP-Kras_G12V (channel shown). 1 μM rapamycin was added at 0 min.

(legend continued on next page)

the frequency of ERK pulses. The lowering of threshold most likely leads to the increased migration, macropinocytosis, and proliferation of cancer cells and it possibly can be used to assess cancer severity as well as a target for intervention.

STAR★METHODS

Detailed methods are provided in the online version of this paper and include the following:

- KEY RESOURCES TABLE
- RESOURCE AVAILABILITY
  - Lead Contact
  - Materials Availability
  - Data and Code Availability
- EXPERIMENTAL MODEL AND SUBJECT DETAILS
  - Cell Lines
- METHOD DETAILS
  - Cell Transfection and Preparation
  - Plasmids Sub-cloning
  - Drugs Preparation
  - Virus Generation
  - Immunoblotting
  - Immunofluorescence
  - Microscopy
  - Computational Modeling
- QUANTIFICATION AND STATISTICAL ANALYSIS
  - Imaging Quantifications
  - Statistical Analysis
- ADDITIONAL RESOURCES

SUPPLEMENTAL INFORMATION

Supplemental Information can be found online at https://doi.org/10.1016/j.devcel.2020.08.001.

ACKNOWLEDGMENTS

The authors thank all members of the Devreotes and Iglesias laboratories as well as members of the Robinson and Iijima laboratories (Johns Hopkins University) and Dr. C. Janetopoulos (University of the Sciences) for helpful suggestions. We thank Dr. S. Schmidt of Losert laboratory (University of Maryland) for writing the MATLAB script for analysis of ERK-KTR changes. We thank Inoue (JHU), Desiderio (JHU), and Balla (NIH) laboratories and AddGene for generous provision of plasmids. We thank D. Biswas of Iglesias laboratory and K. Tian (University for the Creative Arts) for helping with the graphical abstract. This work was supported by NIH grant R35 GM118177 (to P.N.D.), AFOSR MURI FA95501610052 (to P.N.D.), DARPA HR0011-16-C-0139 (to P.N.D. and P.A.I.), K22CA212060 (to C.H.H.), a Cervical Cancer SPORE P50CA098252 Career Development and Pilot Project Award (to C.H.H.), R01GM136711 (to C.H.H.), W. W. Smith Cancer Research Grant (to C.H.H.), NIH grant S10 OD016374 (to S. Kuo of the JHU Microscope Facility), Chinese Ministry of Science and Technology 2016YFA0500202 (to H.C.), and National Natural Science Foundation of China 31770894 (to H.C.).

AUTHOR CONTRIBUTIONS

H.Z. performed the majority of experiments, S.B. conducted computational simulations (Figures 3G and 3H), H.C. performed Kras_G12V CID experiments (Figure 7A), and P.A.I. did the kymograph analysis of Figure 4B. All authors analyzed the data and wrote the manuscript. P.N.D. and C.H.H. supervised the study.

DECLARATION OF INTERESTS

The authors declare no competing interests.

Received: October 30, 2019
Revised: April 30, 2020
Accepted: July 30, 2020
Published: September 1, 2020

REFERENCES

Albeck, J.G., Mills, G.B., and Brugge, J.S. (2013). Frequency-modulated pulses of ERK activity transmit quantitative proliferation signals. Mol. Cell *49*, 249–261.

Aoki, K., Kumagai, Y., Sakurai, A., Komatsu, N., Fujita, Y., Shionyu, C., and Matsuda, M. (2013). Stochastic ERK activation induced by noise and cell-to-cell propagation regulates cell density-dependent proliferation. Mol. Cell *52*, 529–540.

Arai, Y., Shibata, T., Matsuoka, S., Sato, M.J., Yanagida, T., and Ueda, M. (2010). Self-organization of the phosphatidylinositol lipids signaling system for random cell migration. Proc. Natl. Acad. Sci. USA *107*, 12399–12404.

Bae, Y.H., Ding, Z., Das, T., Wells, A., Gertler, F., and Roy, P. (2010). Profilin1 regulates PI(3,4)P2 and lamellipodin accumulation at the leading edge thus influencing motility of MDA-MB-231 cells. Proc. Natl. Acad. Sci. USA *107*, 21547–21552.

Barnhart, E.L., Allard, J., Lou, S.S., Theriot, J.A., and Mogilner, A. (2017). Adhesion-dependent wave generation in crawling cells. Curr. Biol. *27*, 27–38.

Basolo, F., Elliott, J., Tait, L., Chen, X.Q., Maloney, T., Russo, I.H., Pauley, R., Momiki, S., Caamano, J., and Klein-Szanto, A.J.P. (1991). Transformation of human breast epithelial cells by c-Ha-ras oncogene. Mol. Carcinog. *4*, 25–35.

Bement, W.M., Leda, M., Moe, A.M., Kita, A.M., Larson, M.E., Golding, A.E., Pfeuti, C., Su, K.C., Miller, A.L., Goryachev, A.B., and Dassow, G.V. (2015). Activator-inhibitor coupling between Rho signalling and actin assembly makes the cell cortex an excitable medium. Nat. Cell Biol. *17*, 1471–1483.

(B) Time-lapse confocal images of MCF-10A cell expressing Lyn-FRB and FKBP-CDC25 (channel shown). 1 μM rapamycin was added at 0 min.
(C) Time-lapse confocal images of MDA-MB-231 cell expressing Lyn-FRB, FKBP-CDC25, and PH-AKT (channel shown). 1 μM rapamycin was added at 0 min. Also see Video S7.
(D) Time-lapse confocal images of control or Kras_G12V transformed MCF-10A cells expressing LifeAct. Also see Figures S7C–S7F; Video S7 for additional examples.
(E) Quantification of fraction of cells with wave in control or Kras_G12V transformed MCF-10A cells during a 2-h imaging window (mean ± SEM of n = 4 independent experiments, 306 control cells and 347 Kras transformed cells). Unpaired t test with Welch's correction, $p = 0.0071$.
(F and G) Heatmap of ratios of cytosolic to nucleus ERK-KTR signal of control (F) or Kras_G12V transformed (G) MCF-10A cells. n = 25 cells of 2 experiments for each group.
(H) Time-lapse confocal images of M1-M4 MCF-10A cells expressing LifeAct. Also see Video S7 for more examples. Yellow arrows indicate example waves.
(I) Quantification of fraction of cells with wave in M1-M4 MCF-10A cells during a 2-h imaging window (mean ± SD of n = 4 independent experiments, 501 M1 cells, 608 M2 cells, 234 M3 cells, and 302 M4 cells). M2 VS M1: unpaired t test with Welch's correction, $p = 0.0013$; M3 VS M1: unpaired t test, $p < 0.0001$; M4 VS M1: unpaired t test, $p < 0.0001$; M3 VS M2: unpaired t test, $p < 0.0001$; M4 VS M3: unpaired t test, $p = 0.0639$.
The unit of time labeled on images is min and scale bar is 20 μm.

Bhattacharya, S., Banerjee, T., Miao, Y., Zhan, H., Devreotes, P.N., and Iglesias, P.A. (2020). Traveling and standing waves mediate pattern formation in cellular protrusions. Sci. Adv *6*, eaay7682.

Case, L.B., and Waterman, C.M. (2011). Adhesive F-actin waves: a novel integrin-mediated adhesion complex coupled to ventral actin polymerization. PLoS One *6*, e26631.

Dai, C., Whitesell, L., Rogers, A.B., and Lindquist, S. (2007). Heat shock factor 1 is a powerful multifaceted modifier of carcinogenesis. Cell *130*, 1005–1018.

Dawson, P.J., Wolman, S.R., Tait, L., Heppner, G.H., and Miller, F.R. (1996). MCF10AT: a model for the evolution of cancer from proliferative breast disease. Am. J. Pathol. *148*, 313–319.

Diz-Muñoz, A., Thurley, K., Chintamen, S., Altschuler, S.J., Wu, L.F., Fletcher, D.A., and Weiner, O.D. (2016). Membrane tension acts through PLD2 and mTORC2 to limit actin network assembly during neutrophil migration. PLoS Biol *14*, e1002474.

Gerisch, G., Bretschneider, T., Müller-Taubenberger, A., Simmeth, E., Ecke, M., Diez, S., and Anderson, K. (2004). Mobile actin clusters and traveling waves in cells recovering from actin depolymerization. Biophys. J. *87*, 3493–3503.

Gerisch, G., and Ecke, M. (2016). Wave patterns in cell membrane and actin cortex uncoupled from chemotactic signals. Methods Mol. Biol. *1407*, 79–96.

Gewinner, C., Wang, Z.C., Richardson, A., Teruya-Feldstein, J., Etemadmoghadam, D., Bowtell, D., Barretina, J., Lin, W.M., Rameh, L., Salmena, L., et al. (2009). Evidence that inositol polyphosphate 4-phosphatase type II is a tumor suppressor that inhibits PI3K signaling. Cancer Cell *16*, 115–125.

Goulden, B.D., Pacheco, J., Dull, A., Zewe, J.P., Deiters, A., and Hammond, G.R.V. (2019). A high-avidity biosensor reveals plasma membrane PI(3,4)P2 is predominantly a class I PI3K signaling product. J. Cell Biol. *218*, 1066–1079.

Guo, S.T., Chi, M.N., Yang, R.H., Guo, X.Y., Zan, L.K., Wang, C.Y., Xi, Y.F., Jin, L., Croft, A., Tseng, H.-Y., et al. (2016). INPP4B is an oncogenic regulator in human colon cancer. Oncogene *35*, 3049–3061.

Hansen, S.D., and Mullins, R.D. (2015). Lamellipodin promotes actin assembly by clustering Ena/VASP proteins and tethering them to actin filaments. eLife *4*.

Hawkins, P.T., and Stephens, L.R. (2016). Emerging evidence of signalling roles for PI(3,4)P2 in class I and II PI3K-regulated pathways. Biochem. Soc. Trans. *44*, 307–314.

Houk, A.R., Jilkine, A., Mejean, C.O., Boltyanskiy, R., Dufresne, E.R., Angenent, S.B., Altschuler, S.J., Wu, L.F., and Weiner, O.D. (2012). Membrane tension maintains cell polarity by confining signals to the leading edge during neutrophil migration. Cell *148*, 175–188.

Huang, C.H., Tang, M., Shi, C., Iglesias, P.A., and Devreotes, P.N. (2013). An excitable signal integrator couples to an idling cytoskeletal oscillator to drive cell migration. Nat. Cell Biol. *15*, 1307–1316.

Imbalzano, K.M., Tatarkova, I., Imbalzano, A.N., and Nickerson, J.A. (2009). Increasingly transformed MCF-10A cells have a progressively tumor-like phenotype in three-dimensional basement membrane culture. Cancer Cell Int *9*, 7.

Inagaki, N., and Katsuno, H. (2017). Actin waves: origin of cell polarization and migration? Trends Cell Biol *27*, 515–526.

Lam Hui, K., Kwak, S.I., and Upadhyaya, A. (2014). Adhesion-dependent modulation of actin dynamics in Jurkat T cells. Cytoskeleton (Hoboken) *71*, 119–135.

Li, X., Edwards, M., Swaney, K.F., Singh, N., Bhattacharya, S., Borleis, J., Long, Y., Iglesias, P.A., Chen, J., and Devreotes, P.N. (2018). Mutually inhibitory Ras-PI (3, 4) P2 feedback loops mediate cell migration. Proc. Natl. Acad. Sci. USA *115*, E9125–E9134.

Liu, M., Casimiro, M.C., Wang, C., Shirley, L.A., Jiao, X., Katiyar, S., Ju, X., Li, Z., Yu, Z., Zhou, J., et al. (2009). P21Cip1 attenuates Ras- and c-Myc-dependent breast tumor epithelial mesenchymal transition and cancer stem cell-like gene expression in vivo. Proc. Natl. Acad. Sci. USA *106*, 19035–19039.

Malek, M., Kielkowska, A., Chessa, T., Anderson, K.E., Barneda, D., Pir, P., Nakanishi, H., Eguchi, S., Koizumi, A., Sasaki, J., et al. (2017). PTEN regulates PI(3,4)P2 signaling downstream of class I PI3K. Mol. Cell *68*, 566–580.e10.

Manning, B.D., and Toker, A. (2017). AKT/PKB signaling: navigating the network. Cell *169*, 381–405.

Marchesin, V., Montagnac, G., and Chavrier, P. (2015). ARF6 promotes the formation of Rac1 and WAVE-dependent ventral F-actin rosettes in breast cancer cells in response to epidermal growth factor. PLoS One *10*, e0121747.

Martinko, A.J., Truillet, C., Julien, O., Diaz, J.E., Horlbeck, M.A., Whiteley, G., Blonder, J., Weissman, J.S., Bandyopadhyay, S., Evans, M.J., and Wells, J.W. (2018). Targeting RAS-driven human cancer cells with antibodies to upregulated and essential cell-surface proteins. eLife *7*, e31098.

Mebratu, Y., and Tesfaigzi, Y. (2009). How ERK1/2 activation controls cell proliferation and cell death: is subcellular localization the answer? Cell Cycle *8*, 1168–1175.

Mendoza, M.C., Er, E.E., Zhang, W., Ballif, B.A., Elliott, H.L., Danuser, G., and Blenis, J. (2011). ERK-MAPK drives lamellipodia protrusion by activating the WAVE2 regulatory complex. Mol. Cell *41*, 661–671.

Miao, Y., Bhattacharya, S., Banerjee, T., Abubaker-Sharif, B., Long, Y., Inoue, T., Iglesias, P.A., and Devreotes, P.N. (2019). Wave patterns organize cellular protrusions and control cortical dynamics. Mol. Syst. Biol. *15*, e8585.

Miao, Y., Bhattacharya, S., Edwards, M., Cai, H., Inoue, T., Iglesias, P.A., and Devreotes, P.N. (2017). Altering the threshold of an excitable signal transduction network changes cell migratory modes. Nat. Cell Biol. *19*, 329–340.

Nishikawa, M., Hörning, M., Ueda, M., and Shibata, T. (2014). Excitable signal transduction induces both spontaneous and directional cell asymmetries in the phosphatidylinositol lipid signaling system for eukaryotic chemotaxis. Biophys. J. *106*, 723–734.

Pal, D.S., Li, X., Banerjee, T., Miao, Y., and Devreotes, P.N. (2019). The excitable signal transduction networks: movers and shapers of eukaryotic cell migration. Int. J. Dev. Biol. *63*, 407–416.

Peng, G.E., Wilson, S.R., and Weiner, O.D. (2011). A pharmacological cocktail for arresting actin dynamics in living cells. Mol. Biol. Cell *22*, 3986–3994.

Picchini, U. (2007). SDE toolbox: simulation and estimation of stochastic differential equations with MATLAB. http://sdetoolbox.sourceforge.net/.

Regot, S., Hughey, J.J., Bajar, B.T., Carrasco, S., and Covert, M.W. (2014). High-sensitivity measurements of multiple kinase activities in live single cells. Cell *157*, 1724–1734.

Riggi, M., Niewola-Staszkowska, K., Chiaruttini, N., Colom, A., Kusmider, B., Mercier, V., Soleimanpour, S., Stahl, M., Matile, S., Roux, A., and Loewith, R. (2018). Decrease in plasma membrane tension triggers PtdIns(4,5)P2 phase separation to inactivate TORC2. Nat. Cell Biol. *20*, 1043–1051.

Roberts, P.J., and Der, C.J. (2007). Targeting the Raf-MEK-ERK mitogen-activated protein kinase cascade for the treatment of cancer. Oncogene *26*, 3291–3310.

Samatar, A.A., and Poulikakos, P.I. (2014). Targeting RAS–ERK signalling in cancer: promises and challenges. Nat. Rev. Drug Discov. *13*, 928–942.

Santner, S.J., Dawson, P.J., Tait, L., Soule, H.D., Eliason, J., Mohamed, A.N., Wolman, S.R., Heppner, G.H., and Miller, F.R. (2001). Malignant MCF10CA1 cell lines derived from premalignant human breast epithelial MCF10AT cells. Breast Cancer Res. Treat. *65*, 101–110.

Sarbassov, D.D., Guertin, D.A., Ali, S.M., and Sabatini, D.M. (2005). Phosphorylation and regulation of Akt/PKB by the rictor-mTOR complex. Science *307*, 1098–1101.

Sasaki, A.T., Janetopoulos, C., Lee, S., Charest, P.G., Takeda, K., Sundheimer, L.W., Meili, R., Devreotes, P.N., and Firtel, R.A. (2007). G protein–independent Ras/PI3K/F-actin circuit regulates basic cell motility. J. Cell Biol. *178*, 185–191.

Serra, V., Scaltriti, M., Prudkin, L., Eichhorn, P.J.A., Ibrahim, Y.H., Chandarlapaty, S., Markman, B., Rodriguez, O., Guzman, M., Rodriguez, S., et al. (2011). PI3K inhibition results in enhanced HER signaling and acquired ERK dependency in HER2-overexpressing breast cancer. Oncogene *30*, 2547–2557.

Stewart, S.A., Dykxhoorn, D.M., Palliser, D., Mizuno, H., Yu, E.Y., An, D.S., Sabatini, D.M., Chen, I.S.Y., Hahn, W.C., Sharp, P.A., et al. (2003). Lentivirus-delivered stable gene silencing by RNAi in primary cells. RNA *9*, 493–501.

Tang, M., Wang, M., Shi, C., Iglesias, P.A., Devreotes, P.N., and Huang, C.H. (2014). Evolutionarily conserved coupling of adaptive and excitable networks mediates eukaryotic chemotaxis. Nat. Commun. *5*, 5175.

Taniguchi, D., Ishihara, S., Oonuki, T., Honda-Kitahara, M., Kaneko, K., and Sawai, S. (2013). Phase geometries of two-dimensional excitable waves govern self-organized morphodynamics of amoeboid cells. Proc. Natl. Acad. Sci. USA *110*, 5016–5021.

Tanimura, S., and Takeda, K. (2017). ERK signalling as a regulator of cell motility. J. Biochem. *162*, 145–154.

Van Rheenen, J., Song, X., Van Roosmalen, W., Cammer, M., Chen, X., DesMarais, V., Yip, S.C., Backer, J.M., Eddy, R.J., and Condeelis, J.S. (2007). EGF-induced PIP2 hydrolysis releases and activates cofilin locally in carcinoma cells. J. Cell Biol. *179*, 1247–1259.

Vicker, M.G. (2002). F-actin assembly in Dictyostelium cell locomotion and shape oscillations propagates as a self-organized reaction-diffusion wave. FEBS Lett *510*, 5–9.

Wang, M.J., Artemenko, Y., Cai, W.J., Iglesias, P.A., and Devreotes, P.N. (2014). The directional response of chemotactic cells depends on a balance between cytoskeletal architecture and the external gradient. Cell Rep *9*, 1110–1121.

Weiger, M.C., Vedham, V., Stuelten, C.H., Shou, K., Herrera, M., Sato, M., Losert, W., and Parent, C.A. (2013). Real-time motion analysis reveals cell directionality as an indicator of breast cancer progression. PLoS One *8*, e58859.

Weiner, O.D., Marganski, W.A., Wu, L.F., Altschuler, S.J., and Kirschner, M.W. (2007). An actin-based wave generator organizes cell motility. PLoS Biol *5*, e221.

Winans, A.M., Collins, S.R., and Meyer, T. (2016). Waves of actin and microtubule polymerization drive microtubule-based transport and neurite growth before single axon formation. eLife *5*, e12387.

Wozniak, M.A., Kwong, L., Chodniewicz, D., Klemke, R.L., and Keely, P.J. (2005). R-Ras controls membrane protrusion and cell migration through the spatial regulation of Rac and Rho. Mol. Biol. Cell *16*, 84–96.

Wu, Z., Su, M., Tong, C., Wu, M., and Liu, J. (2018). Membrane shape-mediated wave propagation of cortical protein dynamics. Nat. Commun. *9*, 136.

Xiong, Y., Huang, C.H., Iglesias, P.A., and Devreotes, P.N. (2010). Cells navigate with a local-excitation, global-inhibition-biased excitable network. Proc. Natl. Acad. Sci. USA *107*, 17079–17086.

Yang, H.W., Collins, S.R., and Meyer, T. (2016). Locally excitable Cdc42 signals steer cells during chemotaxis. Nat. Cell Biol. *18*, 191–201.

Yang, J.M., Bhattacharya, S., West-Foyle, H., Hung, C.F., Wu, T.C., Iglesias, P.A., and Huang, C.H. (2018). Integrating chemical and mechanical signals through dynamic coupling between cellular protrusions and pulsed ERK activation. Nat. Commun. *9*, 4673.

Ye, X., Chan, K.C., Waters, A.M., Bess, M., Harned, A., Wei, B.R., Loncarek, J., Luke, B.T., Orsburn, B.C., Hollinger, B.D., et al. (2016). Comparative proteomics of a model MCF10A-KRasG12V cell line reveals a distinct molecular signature of the KRasG12V cell surface. Oncotarget *7*, 86948–86971.

STAR★METHODS

KEY RESOURCES TABLE

REAGENT or RESOURCE	SOURCE	IDENTIFIER
Antibodies		
Rabbit anti-phospho-ERK	Cell Signaling Technology	Cat#9101; RRID: AB_331646
Mouse anti-ERK1/2	Cell Signaling Technology	Cat#9107; RRID: AB_10695739
Rabbit anti-phospho-AKT (Ser473)	Cell Signaling Technology	Cat#4060; RRID: AB_2315049
Mouse anti-AKT	Cell Signaling Technology	Cat#2920; RRID: AB_1147620
Anti-mTor	Cell Signaling Technology	Cat#2972; RRID: AB_330978
Anti-Rictor	Cell Signaling Technology	Cat#2140; RRID: AB_2179961
Anti-GAPDH	Cell Signaling Technology	Cat#2118; RRID: AB_561053
Rabbit anti-β-Actin	Cell Signaling Technology	Cat#4970; RRID: AB_2223172
Fluorescent dyes-conjugated goat anti-rabbit	LI-COR	Cat#925-68071; RRID: AB_2721181
Fluorescent dyes-conjugated goat anti-mouse	LI-COR	Cat#925-32210; RRID: AB_2687825
Anti-rabbit IgG_Alexa Fluor® 488 conjugate	Cell Signaling Technology	Cat#4412; RRID: AB_1904025
Anti-mouse IgG_Alexa Fluor® 488 conjugate	Cell Signaling Technology	Cat#4408; RRID: AB_10694704
Chemicals, Peptides, and Recombinant Proteins		
DMEM/F-12 medium	Gibco	Cat#10565042
Horse serum	Gibco	Cat#26050088
EGF	Sigma	Cat#E9644
Cholera toxin	Sigma	Cat#C-8052
Hydrocortisone	Sigma	Cat#H-0888
Insulin	Sigma	Cat#I-1882
DMEM medium	Gibco	Cat#10566024
FBS	Gibco	Cat#16140071
Lipofectamine 3000	Invitrogen	Cat#L3000008
Puromycin	ThermoFisher	Cat#A1113803
Zeocin	ThermoFisher	Cat#R25001
PP242	Sigma	Cat#P0037
Latrunculin A	Enzo	Cat#BML-T119-0100
Ulixertinib	MedChemExpress	Cat#HY-15816
LY294002	Invitrogen	Cat#PHZ1144
ZSTK474	Cell Signaling	Cat#13213
Y27632	Enzo	Cat#ALX-270-333-M001
Latrunculin B	Enzo	Cat#BML-T110-0001
Jasplakinolide	Enzo	Cat#ALX-350-275-C050
Rapamycin	Cayman	Cat#13346
Protease inhibitors	Roche	Cat#11836170001
Phosphatase inhibitor cocktail	Sigma	Cat#P5726
Odyssey Blocking Buffer	LI-COR	Cat#927-50000
Prolong Gold Antifade Reagent	Cell Signaling Technology	Cat#9071
Alexa Fluor® 647 Phalloidin	Cell Signaling Technology	Cat#8940
Experimental Models: Cell Lines		
MCF-10A	M. Iijima Lab (JHU)	N/A
MDA-MB-231	J. Liu Lab (JHU)	N/A
M1 (MCF-10A)	Animal Model and Therapeutic Evaluation Core (AMTEC) of Karmanos Cancer Institute of Wayne State University	N/A
M2 (MCF-10AT1k.cl2)	Same as above	N/A

(*Continued on next page*)

Continued

REAGENT or RESOURCE	SOURCE	IDENTIFIER
M3 (MCF-10CA1h)	Same as above	N/A
M4 (MCF-10CA1a.cl1)	Same as above	N/A
Recombinant DNA		
pFUW2-CFP-Lyn-FRB	This study	N/A
pFUW2-mCherry-FKBP-Inp54p	This study	N/A
pFUW2-mCherry-FKBP-Inp54p (D281A)	This study	N/A
pFUW2-YFP-PH-PLCΔ	This study	N/A
pFUW2-GFP-PH-AKT	This study	N/A
pFUW2-RFP-PH-AKT	This study	N/A
pFUW2-RFP-LifeAct	Lab stock	N/A
pFUW2-Raf-RBD (51-220)-GFP	Lab stock	N/A
YFP-FKBP-CDC25	T. Inoue Lab (JHU)	N/A
RFP-PH-TAPP1	T. Inoue Lab (JHU)	N/A
pFUW2	S. Desiderio Lab (JHU)	N/A
PmdI	S. Desiderio Lab (JHU)	N/A
pRSV	S. Desiderio Lab (JHU)	N/A
pCMV	S. Desiderio Lab (JHU)	N/A
pLenti-GFP-ERKKTR	Regot et al., 2014	Addgene Plasmid #59150
mCherry-FKBP-INPP4B	Goulden et al., 2019	Addgene Plasmid #116864
mCherry-FKBP-INPP4B (C842A)	Goulden et al., 2019	Addgene Plasmid #116865
pBABE-KrasG12V	William Hahn Lab (Dana-Farber) (unpublished)	Addgene Plasmid #9052
pBABE-HrasG12V	William Hahn Lab (Dana-Farber) (unpublished)	Addgene Plasmid #9051
pBABE-C-MYC	Dai et al., 2007	Addgene Plasmid #17758
pUMVC	Stewart, et al., 2003	Addgene Plasmid #8449
pCMV-VSV-G	Stewart, et al., 2003	Addgene Plasmid #8454
psPAX2	Didier Trono Lab (EPFL) (unpublished)	Addgene Plasmid #12260
pMD2.G	Didier Trono Lab (EPFL) (unpublished)	Addgene Plasmid #12259
pLKO.1 scramble shRNA	Sarbassov et al., 2005	Addgene Plasmid #1864
pLKO.1 Rictor_#1 shRNA	Sarbassov et al., 2005	Addgene Plasmid #1853
pLKO.1 Rictor_#2 shRNA	Sarbassov et al., 2005	Addgene Plasmid #1854
pLKO.1 mTOR_#1 shRNA	Sarbassov et al., 2005	Addgene Plasmid #1855
pLKO.1 mTOR_#2 shRNA	Sarbassov et al., 2005	Addgene Plasmid #1856
Software and Algorithms		
Fiji (ImageJ)	http://imagej.nih.gov/ij	Ver 1.52n
MATLAB	https://mathworks.com	Ver R2017a
Graphpad Prism	https://graphpad.com	Ver 7.00
Other		
35 mm glass-bottom dishes	Mattek	Cat#P35G-0.170-14-C
Chambered coverglass	Lab-Tek	Cat#155409PK

RESOURCE AVAILABILITY

Lead Contact

Further information and requests for resources and reagents should be directed to and will be fulfilled by the Lead Contact, Peter N. Devreotes (pnd@jhmi.edu).

Materials Availability

All unique/stable reagents generated in this study are available from the lead contact without restriction.

Data and Code Availability

This study did not generate any unique datasets. The computational simulation codes supporting the current study have not been deposited in a public repository but are available from the corresponding author on request.

EXPERIMENTAL MODEL AND SUBJECT DETAILS

Cell Lines

MCF-10A cells, acquired from Iijima Lab (Johns Hopkins University), were grown at 37°C in 5% CO2 using DMEM/F-12 medium (Gibco, #10565042) supplemented with 5% horse serum (Gibco, #26050088), 20 ng/ml EGF (Sigma, #E9644), 100 ng/ml cholera toxin (Sigma, #C-8052), 0.5 mg/ml hydrocortisone (Sigma, #H-0888) and 10 μg/ml insulin (Sigma #I-1882). MDA-MB-231 cells, acquired from Liu Lab (JHU), were maintained in DMEM medium (Gibco, #10566024) containing 10% FBS (Gibco, #16140071) at 37°C in 5% CO2. M1 (MCF-10A), M2 (MCF-10AT1k.cl2), M3 (MCF-10CA1h), and M4 (MCF-10CA1a.cl1) cells, purchased from the Animal Model and Therapeutic Evaluation Core (AMTEC) of Karmanos Cancer Institute of Wayne State University, were cultured in the same conditions as MCF-10A cells.

METHOD DETAILS

Cell Transfection and Preparation

Transient transfections of the cells were performed using Lipofectamine 3000 (Invitrogen, #L3000008) following manufacturer's instructions. Stable transfected cell lines were selected and/or maintained in culture media containing drugs (2 μg/ml Puromycin, ThermoFisher, #A1113803 and/or 2 mg/ml Zeocin, ThermoFisher, #R25001). Some stable cell lines were sorted by fluorescence tags.

Cells were transferred to 35 mm glass-bottom dishes (Mattek, #P35G-0.170-14-C) or chambered coverglass (Lab-Tek, #155409PK) and allowed to attach overnight prior to imaging. Cells were seeded and incubated at 37°C in 5% CO2 overnight before harvest for immunoblotting, immunofluorescence, or live cell imaging.

For EGF stimulation assays, MCF-10A and MDA-MB-231 cells were usually starved in pure DMEM/F-12, or DMEM medium respectively for 24 hours before stimulation.

Plasmids Sub-cloning

Constructs of CFP-Lyn-FRB, mCherry-FKBP-Inp54p, mCherry-FKBP-Inp54p (D281A), YFP-FKBP-CDC25, YFP-PH-PLCΔ, and RFP-PH-TAPP1 were obtained from Inoue Lab (JHU). GFP/RFP-PH-AKT, RFP-LifeAct, pFUW2, pMDL, pRSV, and pCMV were obtained from Desiderio Lab (JHU). Raf-RBD (51-220)-GFP was obtained from Balla Lab (NIH). pLenti-GFP-ERKKTR (#59150), mCherry-FKBP-INPP4B (#116864), mCherry-FKBP-INPP4B (C842A) (#116865), pBABE-KrasG12V (#9052), pBABE-C-MYC (#17758), pBABE-HrasG12V (#9051), pUMVC (#8449), pCMV-VSV-G (#8454), psPAX2 (#12260) and pMD2.G (#12259) constructs were obtained from AddGene. Lyn-FRB, FKBP-Inp54p, FKBP-Inp54p (D281A), PH-PLCΔ, PH-AKT, LifeAct, and RBD were subcloned to lenti-viral expression plasmid pFUW2. The pLKO.1 knock-down plasmids scramble shRNA (#1864), Rictor_#1 shRNA (#1853), Rictor_#2 shRNA (#1854), mTOR_#1 shRNA (#1855), and mTOR_#2 shRNA (#1856) were obtained from AddGene.

Drugs Preparation

Stocks of 10 mM PP242 (Sigma, #P0037), 25 mM Latrunculin A (Enzo, #BML-T119-0100), 10 mM Ulixertinib (MedChemExpress, #HY-15816), 50 mM LY294002 (Invitrogen, #PHZ1144), 10 mM ZSTK474 (Cell Signaling, #13213), 10 mM Y27632 (Enzo, #ALX-270-333-M001), 25 mM Latrunculin B (Enzo, #BML-T110-0001), 1 mM Jasplakinolide (Enzo, #ALX-350-275-C050) and 10 mM Rapamycin (Cayman, #13346) were prepared by dissolving the chemicals in DMSO. The stocks were diluted to the indicated final concentrations in culture medium or live cell imaging medium. The EGF stock solution was prepared by dissolving EGF (Sigma, #E9644) in 10 mM acetic acid to a final concentration of 1 mg/ml. Insulin (Sigma #I-1882) was resuspended at 10 mg/ml in sterile ddH2O containing 1% glacial acetic acid. Hydrocortisone (Sigma #H-0888) was resuspended at 1 mg/ml in 200 proof ethanol. Cholera toxin (Sigma #C-8052) was resuspended at 1 mg/ml in sterile ddH2O and stored at 4°C. All drug stocks except cholera toxin were stored at -20°C.

Virus Generation

25 ml of 293T cells were seeded at $6x10^5$/ml to 15 cm cell culture dishes on day 1. Conventional calcium phosphate transfection was performed on day 2 to deliver expressing and packaging plasmids into 293T cells. 20 μg pFUW2, 9.375 μg pMDL, 9.375 μg pRSV, 9.375 μg pCMV plasmids (or 10 μg pBABE, 9 μg pUMVC, 1 μg pCMV-VSV-G; or 10 μg pLenti/pLKO.1, 8 μg psPAX2, 2 μg pMD2.G), 250 μl CaCl2 and ddH2O in a total volume of 2.5 ml were mixed with 2.5 ml 2xHEPES (PH=7.05) and incubated for 5 min. The transfection mix was added to the plated cells and shaken gently. Media was changed after 4-6 hours. For virus collection, the medium from infected cells was collected on day 5 and spun at 1000 rpm for 3 min to remove the debris and filtered through 0.45 μm filter followed by ultracentrifugation at 25,000 rpm for 90 min at 4°C in a Beckman ultracentrifuge. The supernatant was discarded and the pellet was dissolved in 70 μl PBS overnight at 4°C to obtain concentrated virus, which was stored as 25 μl aliquots at -80°C.

Immunoblotting

Cells were seeded at 4x10^5 per well in 6-well plates with appropriate growth medium and incubated at 37°C, 5% CO2 overnight, or treated with drugs for indicated period of time before harvesting. Cell lysates were prepared by cell lysis on ice with 3X RIPA buffer containing protease inhibitors (Roche, #11836170001) and phosphatase inhibitor cocktail (Sigma, #P5726). Immunoblotting of individual protein bands was performed by overnight incubating the PVDF membranes with the following primary antibodies (all purchased from Cell Signaling) diluted in 1X Odyssey Blocking Buffer (LI-COR, #927-50000): rabbit anti-phospho-ERK (#9101), mouse anti-ERK1/2 (#9107), rabbit anti-phospho-AKT (Ser473) (#4060), mouse anti-AKT (#2920), anti-mTor (#2972), anti-Rictor (#2140), anti-GAPDH (#2118) and rabbit anti-β-Actin (#4970). Fluorescent dyes-conjugated goat anti-rabbit or anti-mouse antibodies (LI-COR, #925-68071 or #925-32210) were used as secondary antibodies to visualize the protein bands with the Odyssey CLx - LI-COR Imaging System.

Immunofluorescence

Cells were seeded on glass bottom imaging dishes or chambers with appropriate growth medium and incubated at 37°C, 5% CO2 overnight before fixation. 1μM rapamycin was added 1 hour before fixation. Cells were fixed with 4% formaldehyde diluted in warm PBS for 15 min at room temperature. Immunostaining was performed by incubating specimen in appropriate primary antibody in dilution buffer (1X PBS/1% BSA/0.3% Triton X-100) overnight at 4°C and in fluorochrome-conjugated secondary antibody in dilution buffer for 2 hours at room temperature in the dark after 3 PBS rinses. Cells were covered with Prolong Gold Antifade Reagent (Cell Signaling, #9071) and TIRF imaging was done within 24 hours. Primary antibodies for AKT and p-AKT S473 are described in immunoblotting session. Secondary antibodies are anti-rabbit IgG_Alexa Fluor® 488 conjugate (Cell Signaling, #4412) and anti-mouse IgG_Alexa Fluor® 488 conjugate (Cell Signaling, #4408). Alexa Fluor® 647 Phalloidin was purchased from Cell Signaling (#8940).

Microscopy

Total internal reflection fluorescence, wide-field epifluorescence, and confocal microscopy have been described previously (Huang et al., 2013). Briefly, epifluorescence and TIRF microscopy experiments were carried out on a Nikon Eclipse TiE microscope illuminated by an Ar laser (GFP) and a diode laser (RFP). Images were acquired by a photometrics Evolve electron Multiplying Charge-Coupled Device camera (EMCCD) camera controlled by Nikon NIS-Elements. Confocal microscopy was carried out on Zeiss AxioObserver inverted microscope with either LSM780-Quasar (34-channel spectral, high-sensitivity gallium arsenide phosphide detectors, GaAsP) or LSM800 confocal module controlled by the Zen software. All live cell imaging was carried out in a temperature/humidity/CO2-regulated chamber.

Computational Modeling

The wave simulations were based on excitable system with global and local perturbations. The excitable waves were modeled through reaction-diffusion equations (Xiong et al., 2010). The signal transduction excitable network (STEN) was set up as an activator (X)-inhibitor (Y) system as shown below:

$$\frac{\partial X}{\partial t} = D_X \nabla^2 X - (a_1 + a_2(Y - S_{in}))X + \frac{a_3 X^2}{a_4^2 + X^2} + a_5 + U_N$$

$$\frac{\partial Y}{\partial t} = D_Y \nabla^2 Y + \varepsilon(-Y + c_1 X)$$

The non-linear term in the first equation contributes to positive feedback while the epsilon (ε) in the second equation creates a delay in the response of the inhibitor. When the activator receives a supra-threshold stochastic input, the autocatalytic feedback leads to a sharp rise in activity, creating the wave front (green in Figures 3G and 3H). The inhibitor, albeit slowly, accumulates to ultimately subdue the activator concentration – creating the wave back (red in Figures 3G and 3H). After the inhibitor subdues the activator response, it then decays back to resting concentration, resulting in a refractory period. When coupled with diffusion across adjacent excitable elements, this creates a propagating wave.

Simulations were done using a two-dimensional 200x200 array in MATLAB, using stochastic differential equations (Picchini, 2007). The term U_N incorporates the stochastic input to the system which is modeled as a zero-mean Gaussian white noise process (σ). The parameter values used are: a_1 = 0.167, a_2 = 16.67, a_3 = 167, a_4 = 1.2, a_5 = 1.47, ε = 0.12, c_1 = 39, D_X = 2.2, and D_Y = 1.2.

External stimulus to the excitable system is provided through the term S_{in} in the activator equation. In the absence of a stimulus, this term was set to zero. For a global stimulus, the term was set to 0.2 for the whole 200x200 system. For a gradient simulation, a Gaussian profile was used for S_{in}, with mean at the bottom edge of the spatial array, and a standard deviation of 60 – with the amplitude rising from 0 to 0.5.

QUANTIFICATION AND STATISTICAL ANALYSIS

Imaging Quantifications

Cell Area Quantification

Single cells were first manually tracked and cropped out from a pool of cells in the movies, and converted into binary images using normal ImageJ procedures (despeckle, threshold, and fill-holes). The relative value of cell area for each frame of the movie was obtained basing on the processed binary images.

Wave Quantification

First, we only quantified the waves which initiate and travel in the internal region of the cell basal surface. We did not define the protrusion events seen in cells as our travelling waves, thus we did not count protrusion events for our wave quantification. Second, we quantified travelling but not standing waves. Third, the duration of wave was defined as the lifetime of the wave from its appearance to its disappearance. When a wave splits, the clock keeps going until the longest lasting portion disappears. When a wave merges with another one, the time of the origin of that wave to the disappearance of the merged wave is counted as its duration. The (maximum) width is the maximum length of the lateral span of a wave during its lifetime. The velocity is the average velocity of all parts of a specific wave.

Lamellipodia Kymograph

In Figure 4B, the lamellipod was defined as the higher intensity of signal of FKBP channel after rapamycin-induced recruitment. This signal was much lower in the cytosol region, because lamellipodia has two layers of membrane where FKBP has been recruited. For frames before the addition of rapamycin, the profile of the ring in the first frame after the recruitment is used since the cell shape has not changed before the recruitment. A line perpendicular to the tangent of the cytosol boundary is drawn at each angle from 0 to 360 degree. The length of lamellipodia at each angle is measured along this line. The kymograph was generated by aligning these values versus time.

Statistical Analysis

GraphPad Prism 7 software was used for all statistical analyses. All quantifications are displayed as mean ± SD or SEM. Two-tailed P-values were calculated using parametric t test. $P<0.05$ was considered statistically significant. Further details of statistical parameters and methods are reported in the corresponding figure legends.

ADDITIONAL RESOURCES

No additional resources.